The top-of-atmosphere, surface and atmospheric cloud radiative kernels based on ISCCP-H datasets: method and evaluation

Yuanchong Zhang[12†], Zhonghai Jin[2] and Monika Sikand[3,4]

[1]SciSpace LLC, 2880 Broadway, New York, NY 10025, USA.

[2] NASA Goddard Institute for Space Studies, 2880 Broadway, New York, NY 10025, USA.
[3] Department of Engineering, Physics, and Technology, Bronx Community College, CUNY, NY, 10453, USA.

[4]Department of Applied Physics and Applied Mathematics, Columbia University, New York, NY 10027, USA.

Corresponding author: Yuanchong Zhang (yz7@columbia.edu)

Key Points:

- The cloud radiative kernel datasets are created for longwave, shortwave and their sum, net, respectively, at the top of atmosphere, the surface and in the atmosphere. They are evaluated by direct comparison with the counterparts of the other three representative datasets and with the cloud radiative effects from the Clouds and the Earth's Radiant Energy System products. In addition, the kernel-derived cloud feedback is also directly compared with the previous ensemble results from 10 climate models and the observation-based results from the Clouds and the Earth's Radiant Energy System products. Both comparisons well-validated our cloud kernels and their derived cloud feedback.
- The uncertainty budget for cloud kernel-derived cloud feedback at the top of atmosphere is estimated based on uncertainties of cloud kernels and cloud fraction change from the direct comparisons. It shows that the cloud fraction change associated uncertainty contributes > 98.5% of the total cloud feedback uncertainty while cloud kernels' is very small. We have also tested the effect of dry bias of water vapor on the cloud radiative kernel calculation when the clear-sky water vapor is used for the cloud-free layers under cloud layers and estimated error/uncertainty may be caused in the calculation by such a dry bias. The results show such-caused errors/uncertainties are in high order and need not to be taken into account at present.
- Our preliminary evaluation also shows that some near-zero or small cloud feedback in the top-of-atmosphere-alone feedback results from the compensation of sizable cloud feedback of the surface and atmospheric feedback. It demonstrates how the surface and atmospheric cloud kernel-derived cloud feedback can be used to reveal some significant surface and atmospheric cloud feedback whose sum appears insignificant in the top-of-atmosphere-alone feedback. In addition, the ATM LW cloud feedback may play a role in enhancing meridional atmospheric energy transport.

Abstract

This study aims to create observation-based cloud radiative kernel (CRK) datasets and evaluate them by direct comparison of CRK and the CRK-derived cloud feedback datasets. Based on the International Satellite Cloud Climatology Project (ISCCP) H datasets, we calculate CRKs (called ISCCP-FH or FH CRKs) as 2D joint function/histogram of cloud optical depth and cloud top pressure for shortwave (SW), longwave (LW), and their sum, Net, at the top of atmosphere (TOA), as well as, for the first time, at the surface (SFC) and in the atmosphere (ATM). With cloud fraction change (CFC) datasets from doubled-CO_2 simulation and short-term observational anomalies, we derive all the TOA, SFC and ATM cloud feedback for SW, LW and Net using our CRKs.The direct comparison with modelled and observed CRKs (or cloud radiative effects), cloud feedback from previous model results and the Clouds and the Earth's Radiant Energy System products show that our CRKs and CRK-derived cloud feedback are reasonably well validated. We estimate the uncertainty for the CRK-derived cloud feedback and show that the CFC-associated uncertainty contributes > 98.5% of the total cloud feedback uncertainty while CRK's is very small. Our preliminary evaluation also shows that some near-zero/small cloud feedback in the TOA-alone feedback indeed results from the compensation of sizable cloud feedback of the SFC and ATM feedback and reveals some significant surface and atmospheric cloud feedback whose sum appears insignificant in TOA-alone feedback. In addition, the ATM LW cloud feedback seems to play a role in enhancing meridional atmospheric energy transport.

Plain Language Summary

(optional)

1 Introduction

The notion of feedback is referred to internal, mutually interacting processes in nature and was introduced to climate literature in the 1960s (Manabe, 1969). In the past two decades, the radiative kernel technique has become a useful tool in studying climate feedback (Shell et al., 2008). A climate radiative kernel represents a differential radiative response to a climate variable's change from a reference (control) state. For climate feedback, the change of the net radiative flux effect (or forcing) at the top of atmosphere (TOA), $\Delta(Q - F)$, is usually concerned, where Q is the absorbed shortwave (SW) radiation by the earth-atmosphere system and F is outgoing longwave (LW) radiation (OLR) (Soden et al., 2008). With the assumption that no interactions or nonlinear responses among the various climate processes are permitted, we may describe the radiative kernel approach for climate feedback using,

$$\gamma = \frac{\Delta(Q-F)}{\Delta T_s} = \sum_i \frac{\partial(Q-F)}{\partial X_i}\frac{dX_i}{dT_s} = \sum_i K_{x_i}\frac{dX_i}{dT_s} = \sum_i \gamma_i \quad (1)$$

where, γ is the total climate feedback, the sum of individual feedback terms, γ_i, which may be decomposed into two parts, the radiative kernel, $K_{x_i} = \frac{\partial(Q-F)}{\partial X_i}$, the rate of change of the TOA net flux with respect to climate variable, X_i, and, $\frac{dX_i}{dT_s}$, the rate of change of the climate variable, X_i, with respective to T_s, the surface air temperature. This separation facilitates climate feedback estimate because radiative kernels are usually calculated offline based on mean climate state and relatively insensitive to a particular mean climate state, compared to the intermodal differences in climate response (Soden et al., 2008). When a non-cloud climate variable's rate of change, $\frac{dX_i}{dT_s}$, is available, its feedback can readily be obtained from the product of $K_{x_i}\frac{dX_i}{dT_s}$.

However, the above kernel approach cannot simply be applied to cloud radiative kernel (CRK) and cloud feedback because of their high nonlinearity with respect to cloud properties. Cloud feedback has traditionally been estimated through the partial radiative perturbation (PRP) method, "cloud forcing" analysis approach and the online feedback suppression approach (Bony et al., 2006). Soden and Held (2006) used the "residual" method and later Soden et al. (2008) used the "adjusting" method to indirectly estimate cloud feedback using non-cloud radiative kernels (for atmospheric temperature and humidity, water vapor, surface albedo, etc.). The cloud radiative kernel was not explicitly created and directly used in estimating cloud feedback until Zelinka et al. (2012, thereafter Z2012) introduced 49 cloud types (bins) in defining and calculating CRK and cloud feedback based on 7 x 7 2D joint function/histogram of cloud optical depth (τ, as X) and cloud top pressure (CTP, as Y, see Figure 1). The histogram is modified from

the original 6 x 7 τ-CTP histogram, used in the International Satellite Cloud Climatology Project (ISCCP) (Rossow and Schiffer, 1999). The Z2012's method may be taken as a kind of linearization on τ and CTP for the CRK approach in estimating cloud feedback using $K_i \frac{dX_i}{dT_s}$, where K_i is the CRK and dX_i is the cloud change for the *ith* bin, and the summation of *i* over all the 49 cloud types (bins) gives the total cloud feedback for a grid cell. Note that Chen et al. (2000) introduced and calculated "overcast cloud change flux" that has the same physical definition as the CRK but for a coarser (3 X 3) τ-CTP histogram and without introducing the notion of 'cloud radiative kernel'.

Since Z2012, there have appeared a number of literatures (Yue et al., 2016; Zhou et al., 2013 and Berry et al., 2019) using Z2012's method to produce CRKs, with which to estimate cloud feedback. The CRKs may be GCM based, observation based or their combination. As the Cloud Feedback Model Intercomparison Project (CFMIP) Observation Simulator Package (COSP) software (Bodas-Salcedo et al. 2011) is implemented in GCMs, using COSP-ISCCP simulated cloud changes on τ -CTP histogram with CRKs has become a feasible tool for (directly) estimating GCMs' cloud feedback.

In this study, we focus on the calculation and evaluation of our cloud radiative kernels and their derived cloud feedback. Section 2 describes the method for calculating the CRKs based on the ISCCP H-series (ISCCP-H) products (Young et al. 2018) for both TOA and surface (SFC), and their differences, atmosphere (ATM). Section 3 describes features of the TOA, SFC and ATM CRKs. Section 4 compares the ISCCP-H based TOA CRKs and three representative TOA CRK sets to evaluate our TOA CRKs as well as estimate uncertainties of TOA CRKs. Section 5 estimates the TOA cloud feedback uncertainty budget based on the uncertainties of CRKs and cloud fraction change (CFC) from GCMs. Section 6 describes and evaluates the TOA,

SFC and ATM cloud feedback results derived using our CRKs and reports the preliminary findings from this study. Section 7 presents a further evaluation by comparing our cloud radiative kernel derived cloud radiative effects and cloud feedback with the results derived from the data products of the Clouds and the Earth's Radiant Energy System (CERES, Wielicki et al., 1996). Section 8 summarizes this study and draws conclusions. In Appendices A and B, we report the results of the sensitivity tests for quantifying how much uncertainty may be caused in our CRK calculation by the dry-bias of water vapor under cloud layers and by different cloud thickness specifications, respectively.

Figure 1

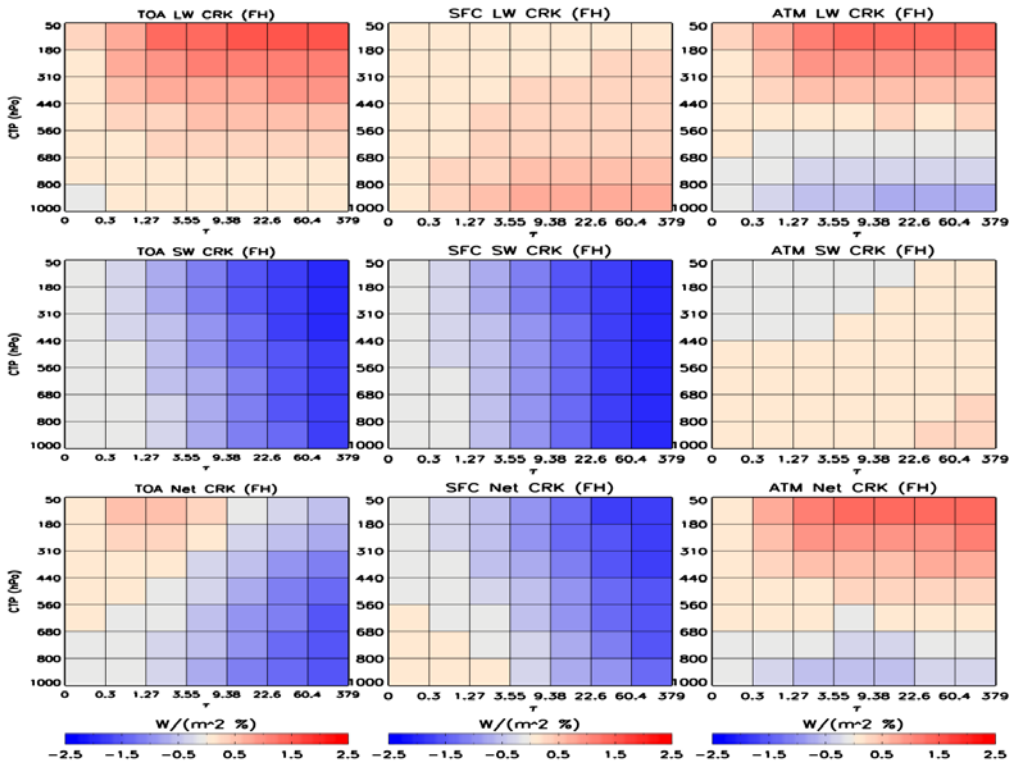

Figure 1. Global, annual mean cloud radiative kernels, calculated using the ISCCP-FH code, for 49-bin histogram: the three (left to right) columns are for TOA, surface (SFC) and in atmosphere (ATM), respectively, and the three (top to bottom) rows are for LW, SW and Net, respectively, in Wm^{-2} $\%^{-1}$. The CRKs are the overcast cloud radiative effects (OCRE), divided by 100 for overcast (100%) cloud amount (Section 2); positive sign means radiative heating in the system (the earth-atmosphere, earth or atmospheric system for TOA, SFC or ATM, respectively), see Section 2 for details.

2 Method to calculate cloud radiative kernels.

We use the ISCCP-FH flux production code to calculate our cloud radiative kernels (called ISCCP-FH or FH CRKs). The code has been used to produce radiative profile fluxes in 3-hourly on 110-km equal-area map for 1983 to 2017 (Zhang et al., 2021). It is modified from the radiation code of the GCM of the NASA Goddard Institute for Space Studies (GISS), ModelE2 (Schmidt et al., 2006), and it is equivalent to the radiation code of ModelE2.1 (Kelley et al., 2020). The ISCCP-FH radiation code is designed to be detailed, self-consistent and as realistic as possible, in which, SW (0.2 – 5.0 μm) and LW (5.0 – 200 μm) are all treated using the correlated k-distribution method and the atmospheric and surface properties are from consistent data sources. It has an accuracy of 1 Wm^{-2} for cooling rates (in degree/day) throughout the troposphere and most of the stratosphere (Lacis and Oinas, 1991) for LW and close to 1% for SW. The main input datasets for the ISCCP-FH code are from ISCCP-H products (Young et al. 2018). Through 1-yr, monthly and (110 km) regional comparison with CERES and the Baseline Surface Radiation Network (BSRN, Ohmura, 2014) observations for TOA and surface, respectively (Zhang et al., 2021), it shows that the uncertainties are ≤ 10 Wm^{-2} at TOA and ≤ 20 Wm^{-2} at surface for the monthly, regional mean ISCCP-FH fluxes, which is slightly better than its precursor, the ISCCP-FD products (Zhang et al., 2004), but the former has higher spatial resolution of 110 km than the latter's 280 km.

For CRK calculation, the only major change of the code is that the ISCCP-H's original, 3-hourly (up to) 18 types of clouds are now replaced by 49 individual types of clouds as appearing in the 49-bin histogram (Figure 1) with the specified τ, CTP and cloud amount (as defined in Z2012, see below), whose values are invariant in the 3-hourly calculation. All the other input parameters essentially remain the same as those used in the ISCCP-FH flux production. Specifically, 3-hourly temperature/humidity profiles, surface properties (visible

albedo, skin temperature, etc.) and daily snow/ice data are from the ISCCP-H datasets. The daily total solar irradiance (TSI) is based on the Solar Radiation and Climate Experiment (SORCE, V-15) datasets, equivalent to that used in CERES. Monthly aerosol climatology for all the actual years is from Max Planck Institute Aerosol Climatology, version 2 (MAC-v2, Kinne et al., 2019). All the gases are the same as ModelE2's except 3-hourly humidity (precipitable water) profile and column ozone that are also from ISCCP-H (for list of all main input parameters other than τ and CTP, see Text S1 in supporting Information, SI).

Clouds are specified as overcast (100% cover) in order to produce overcast cloud radiative effects (OCRE), for which the overcast-sky net flux replaces the original, all-sky net flux in conventional CRE (defined as the net radiative flux difference between all sky and clear sky). The OCRE is calculated for SW, LW and their sum, Net (total), respectively, at TOA and surface for TOA and SFC CRK, respectively. To save CPU time, we make radiatively linear average of τ and CTP of the four corners for each of the 49 bins to obtain a radiatively linearly averaged center (not equal to geometrically averaged center) by using ISCCP's counts-physical conversion tables for τ and pressure (CTP), where the conversion tables are for radiatively linearly averaging physical parameters that are nonlinear with radiation (Young et al, 2018; Rossow et al, 1996). Such obtained center's τ and CTP values are then used to calculate flux for the bin, which is equivalent to Z2012's 4-corner flux average for the bin. The model sets the ISCCP-H's original relative humidity (from nnHIRS, see Young et al, 2018) to 100% for cloud layers for (overcast) cloudy scene (see Appendix A for explanation). Cloud particle sizes for liquid and ice are based on monthly climatology from Han et al. (1994 and 1999). The ice phase in a cloud layer is defined when the temperature at CTP and cloud base are < 260 K and < 273.15 K, respectively; otherwise, the model sets to the liquid clouds. The cloud vertical

structure used in the ISCCP-FH production is turned off as single-layer clouds are now used in consistency with the usage of the COSP-ISCCP simulation. The cloud thickness (therefore cloud base) is a cubic polynomial function of CTP with its coefficients as function of cloud optical thickness τ, longitude, latitude, ocean/land, and month, based on linear least square fitting for a combination of the 20-year rawinsonde climatology (Wang et al., 2000) and 5-year climatology from the CloudSat and CALIPSO data products (Stephens, et al., 2002; Winker et al., 2003) (see Figures S1 and S2 in SI for cloud thickness/base examples) Clear-sky fluxes are calculated by setting cloud fraction = 0 and τ = 0 (without water vapor saturation), which only needs to be calculated once for each grid cell. The different treatments of water vapor for cloudy and clear sky are physically consistent with GCM models' clouds generating process. The water vapor saturation for cloud layers may be taken as the cloud-masking effect and thus our CRKs include this effect.

In short, all the input atmospheric (including cloud's) and surface property parameters are in 3-hourly (but 100% cloud amount, CTP and τ are temporally invariant for each single-layer cloud type) with the exceptions of cloud particle size, cloud thickness and aerosols that are based on monthly climatology, and TSI, column ozone and snow/ice that are based on daily observation as well as all the gases (excluding water vapor and ozone) that remain the models' original setting.

In the calculation, the TOA CRK, $K_{x_i} = \frac{\partial(Q-F)}{\partial X_i}$, is separated into two terms, $\frac{\partial(-F)}{\partial X_i}$ for LW, and $\frac{\partial(Q)}{\partial X_i}$ for SW, respectively, and their sum is the Net CRK. The ∂X_i here is the cloud fraction change (CFC). All the CRKs are divided by 100 so they become a differential change of OCRE with respect to 1% CFC, expressed in $Wm^{-2}\ \%^{-1}$. The calculation is conducted 3-hourly

for each of the 49 cloudy scenes/type (bins) plus one clear-sky scene (totally 50 scenarios) separately for each grid cell on 110-km global equal-area map. Note that each bin's CRK value is calculated for that type of clouds alone as if the rest types of clouds are not present in a grid cell.The primary consideration for the high-temporospatial resolution calculation is that our CRKs should be as realistic as possible, and their monthly (and annual) means should be a better representation of the true global, monthly mean as they are averaged over CRKs based on all the conditions (3-hourly of day and various atmospheric and surface properties) compared with those CRKs based on monthly and zonal mean atmospheric and surface properties.

The TOA formula may be extended to the surface and atmosphere with the OCRE definition at TOA. To do so, we first note that, in the conventional definition (Ramanathan et al., 1989), cloud effects (or 'forcing') is defined as the difference of the net radiative heating (NTRH) for the earth-atmosphere system between all and clear sky (which may be divided into the SW and LW parts). Therefore, to be consistent with the conventional definition, we can rewrite Q as $NTRH_{sw_toa}$ and (– F) as $NTRH_{lw_toa}$, for the earth-atmospheric system's SW and LW, respectively, and explicitly divide them into the SFC and ATM components for the separated earth (SFC) and atmospheric (ATM) system, respectively (positive sign for heating in a system), i.e.,

$$NTRH_{sw_toa} = NTRH_{sw_sfc} + NTRH_{sw_atm} \tag{2a}$$

and

$$NTRH_{lw_toa} = NTRH_{lw_sfc} + NTRH_{lw_atm} \tag{2b}$$

Thus we have linearly decomposed the TOA SW and LW net fluxes into two parts for SFC and ATM, i.e., for the two entities, the earth (without atmosphere) and atmospheric system, respectively. The sum of Eqs. (2a) and (2b) yields the decomposition equation for Net (not

shown). The decomposition is physically and mathematically justified that can be applied to theCRE (cloud forcing), OCRE (for CRK) and cloud feedback calculation. We write the decomposition equation for OCRE,

$$\mathrm{OCRE}_{\mathrm{toa}} = \mathrm{OCRE}_{\mathrm{sfc}} + \mathrm{OCRE}_{\mathrm{atm}} \tag{2c}$$

which can now be for LW, SW or Net after dropping their subscripts. If we divide all the terms in Eq. (2c) by 100 for overcast cloud fraction, the eqation becomes the CRK's decomposition Equations for a cloud type (bin),

$$\mathrm{CRK}_{\mathrm{toa}} = \mathrm{CRK}_{\mathrm{sfc}} + \mathrm{CRK}_{\mathrm{atm}} \tag{2d}$$

Multipling Eq. (2d) by CFC/dTs yields the decomposition equation for cloud feedback for a bin, for which, we make summation over 49 types of clouds and we deduce the decomposition equation for cloud-type-based cloud feedback using $K_i \frac{dX_i}{dT_s}$ (Section 1),

$$\begin{aligned} FDBK_{cld_TOA} &= \frac{1}{dTs}\sum_{i=1}^{49} CRKtoa_i \times CFC_i \\ &= \frac{1}{dTs}\sum_{i=1}^{49} CRKsfc_i \times CFC_i + \frac{1}{dTs}\sum_{i=1}^{49} CRKatm_i \times CFC_i \\ &= FDBK_{cld_SFC} + FDBK_{cld_ATM} \end{aligned} \tag{2e}$$

where $FDBK_{cld_TOA,}$ $FDBK_{cld_SFC\ and}$ $FDBK_{cld_ATM,}$ are total cloud feedback for a grid cell for TOA, SFC and ATM, respectively. Eq. (2e) can be used for LW, SW or Net. The summation of *i* is over the 49 cloud types and 1/*dTs* is moved out of the summation sign because it is in global mean (not function of cloud type or grid cell). Note that, in deriving Eqs. (2a), (2b), (2c), (2d) and (2e), we have only used linear operators without introducing any nonlinear operation.

After calculating CRKs for TOA and SFC, we can have the ATM CRK by differencing using Eq. (2d).. Similarly, we can obtain the ATM cloud feedback using Eq. (2e).

Both the TOA and SFC CRKs are directly calculated in 3-hourly on 110-km equal-area map for year 2007. We have also produced the ATM CRKs. To our knowledge, SFC and ATM CRKs have not been published at the time of writing (though non-cloud SFC and ATM radiative kernels have been produced in the past few years, e.g., Kramer et al., 2019). As explained above, the SFC and ATM CRKs are just the two components decomposed from the TOA CRKs. The original 3-hourly and 110-km kernel data is averaged to monthly (and annual) means and regridded to 250-km equal-area map which is also replicated to 2.5° longitude x 2.0° latitude equal-angle map for the majority of GCM-related uses. This coarser version of the ISCCP-FH cloud radiative kernel datasets (DOI: 10.5281/zenodo.4677580) can be downloaded from https://zenodo.org/record/4677580#.YHDsaDwpCUk.

3 ISCCP-H based TOA, surface and atmospheric cloud radiative kernels.

Figure 1 shows the global, annual mean FH CRKs for 49-type clouds (bins) on the 7 x 7 histogram (X = τ and Y = CTP) for (Left to Right) TOA, SFC and ATM in 3 columns, respectively; each column is for (top to bottom) LW, SW and Net, respectively. For a better illustration, we plot Figure 2a (2b) for the 7 rows (columns) of Figure 1's CRKs as 7 individual functions of τ (CTP) to represent Figure 1's each panel's 2D function, CRK(τ,CTP), in the same matrix order. We will not specify which panel of Figure 2a or 2b is compared with the panel of Figure 1 unless the two panels in comparison are not for the same panels in their own matrices.

Figure 2a.

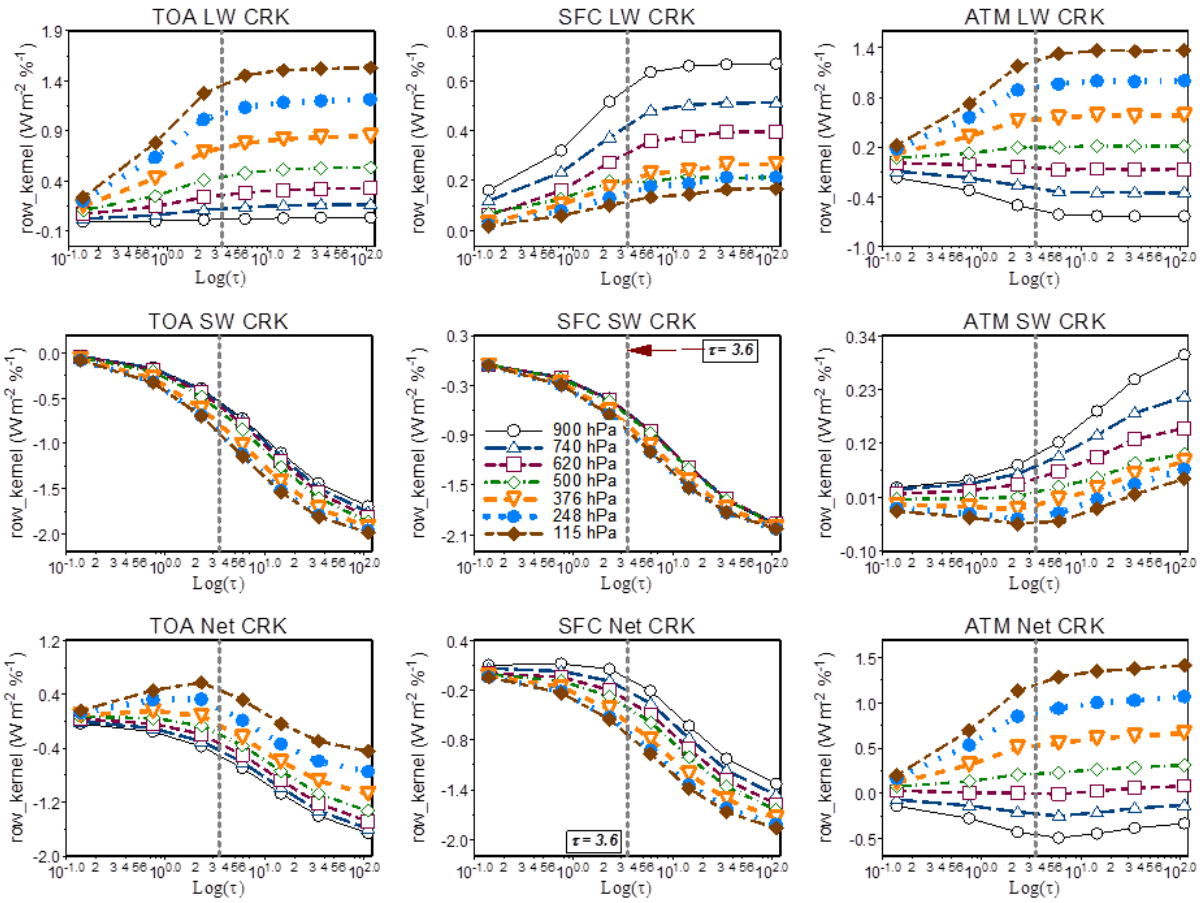

Figure 2a. Seven rows of CRK ('row_kernel') of each panel of Figure 1, as function of τ (in Log scale with base of 10). The legend (in the central panel) shows radiatively linearly averaged center's CTP for each row_kernel. The vertical line in each panel (indicated by an arrow in the central panel) is for τ = 3.6.

Figure 2b.

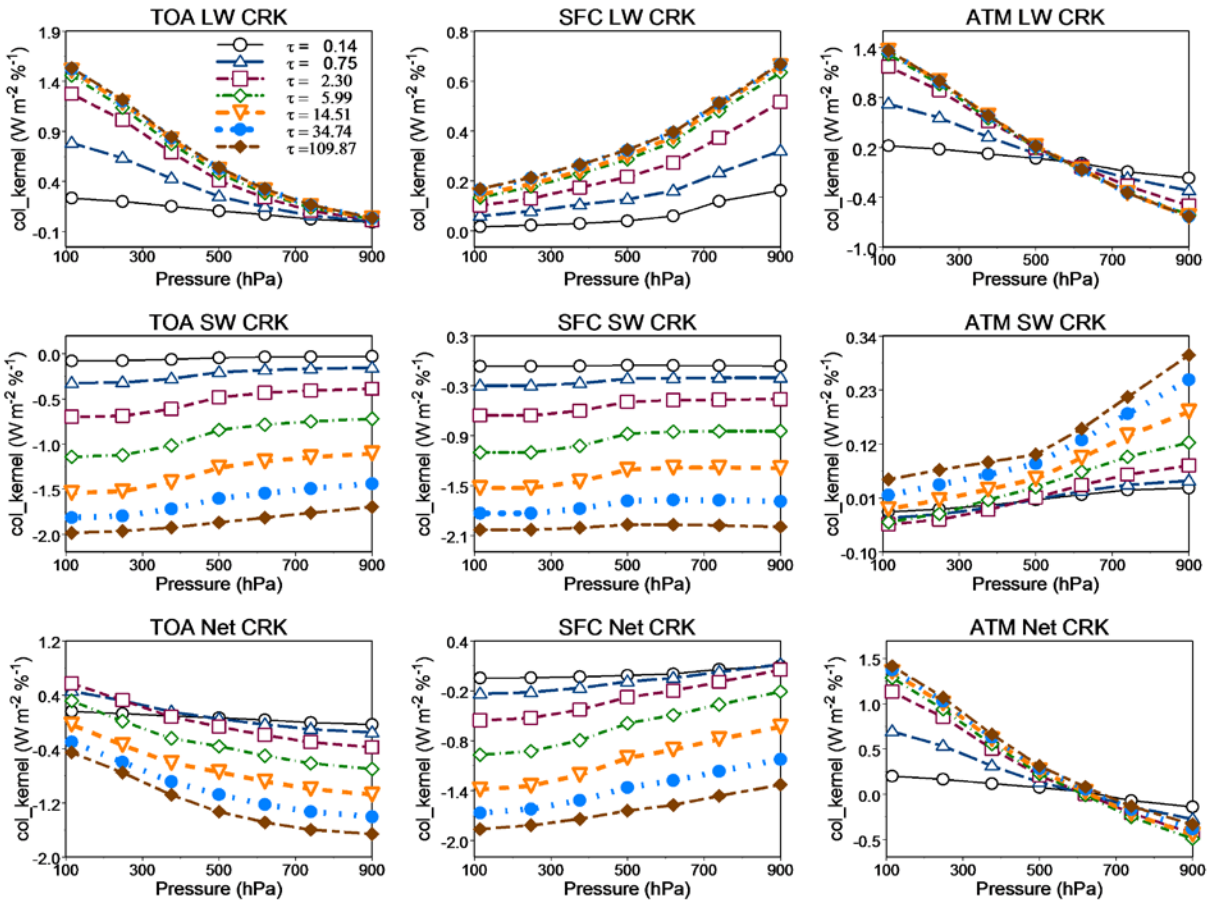

Figure 2b. Seven columns of CRK ('col_kernel') of each panel of Figure 1, shown as function of pressure. The legend (in the top left panel) shows radiatively linearly averaged center's τ for each column.

In Figure 1, the 3 (left) TOA panels for LW, SW and Net CRKs are highly similar to the ensemble counterparts of (Figure 1 of) Z2012. The features described there have reappeared here, such as the LW CRK bins are all positive while all the SW CRK bins are negative and LW CRK is sensitive to both τ and CTP for thin clouds ($\tau < 3.6$), but when $\tau \gtrsim 3.6$, LW CRK

becomes insensitive to τ because of saturation (cf. Figure 2a). We do not repeat what has been described in Z2012 but emphasize the following.

The TOA LW CRK essentially depends on how much the surface emission (to TOA) is absorbed and emitted/reemitted (towards both TOA and surface) by clouds (greenhouse effects) in reducing OLR, in which CTP has a dominant role (CTP largely determines the effective cloud top temperature and OLR; higher clouds have lower top temperature and OLR, and therefore larger CRK, and vice versa) while τ has a secondary role (especially when $\tau \gtrsim 3.6$), showing a generally horizontal layered structure (cf. Figure 2a). In contrast to LW, the SW CRK's magnitude (in negative) essentially depends on how much TOA-incoming SW radiation is reflected by clouds, in which column τ has a dominant role while CTP plays a secondary role, showing a generally vertically layered structure (cf. Figure 2b). As a result, the TOA Net panel shows their combined structure: roughly antisymmetric with respect to the diagonal line from the low left corner to the upper right corner; most of bins above (below) the line are positive (negative).

Figure 1's middle column shows the SFC CRKs for (top to bottom) LW, SW and Net, respectively. The LW CRK panel shows that all the bins are also positive. The near-surface clouds most effectively trap the upward terrestrial emission for surface to absorb so the largest SFC LW CRK values appear in the lowest cloud layer, somewhat like an upside-down of the TOA LW CRK panel but with magnitude reduced by ~1/2 (cf. Figures 2a and 2b). The SFC LW CRK decreases with cloud height for each τ column, opposite to the TOA's (cf. Figures 2a and 2b). This decrease is mainly because the cloud base of higher clouds has lower temperature and emits less toward the surface, resulting in less emission to reach the surface. It also increases as τ increases for each CTP row before reaching $\tau \approx 3.6$ but then increase slowly (saturated, cf.

Figure 2a). The SFC SW panel is similar to the TOA's since column τ plays a dominant role for both of them (cf. Figure 2b), and to a second degree, its magnitude also has small increase with height (cf. Figures 2b and 2a) because of small atmospheric absorption through the cloud-free layers (under clouds) so there is less SW flux to reach the surface (larger magnitude in negative). The SFC Net CRK panel seems somewhat like an upside-down of the TOA Net CRK panel and roughly appears antisymmetric with respect to the diagonal line from the upper left corner to the lower right corner; most of the bins above (below) the line are now negative (positive) (cf. Figures 2a and 2b). The sign of each bin depends on the competition between LW and SW CRK values. Overall, SW outweighs LW, so all the bins have negative values except six bins at the low left corner for the SFC Net CRK.

The right column in Figure 1 is for the ATM CRKs, determined by the difference between the TOA and SFC CRKs. The ATM LW CRK essentially depends on how much of the sum of upward surface emission and downward emission (from clouds and other atmospheric constituents) can possibly be absorbed by the atmosphere (including clouds) and it shows a generally horizontally-layered structure (cf. Figure 2a) like the TOA and SFC' LW CRKs, indicating CTP's dominance. For the same τ column, the lower a CTP level of a bin is, the more upward surface emission is absorbed and reemitted back to the surface by the cloud layer (with the CTP) and the less available LW flux that can possibly get through the cloud layer and absorbed by the rest of the atmospheric column (above the cloud layer) such that it becomes so small that the whole atmospheric column's absorption is even smaller than the clear-sky counterpart , resulting in negative ATM LW CRK for near-surface clouds. This sign change is clearly shown in Figure 2b. The saturation for $\tau \gtrsim 3.6$ is still present (cf. Figure 2a). The ATM SW CRK (middle panel) is much smaller than both the TOA and SFC SW CRKs because of

cancellation in their differencing. Noticeably, the three low-right-corner bins of the panel have the largest positive values because of both the strong absorption and the strong reflection of incoming solar radiation by low, thick-τ clouds. The strong reflection makes more solar radiation available for the cloud-free layers (above the cloud layer) to absorb (compared with clear sky) so the absorption by the whole atmospheric column (with clouds included) has the largest CRK values. The (bottom) panel for ATM Net in Figure 1 is the superposition of the above ATM LW and SW CRKs, of which, the former is dominant, and, as a result, it is somewhat like ATM LW CRK, showing that almost all the high and middle clouds (CTP < 680 hPa) heat the atmosphere while the rest clouds have cooling effects on the atmosphere (cf. Figure 2a and 2b).

All the features of the FH CRKs described above are qualitatively consistent with our observations and physical understanding for cloud radiative effects at TOA, surface and in atmosphere, reflecting self-consistency of the ISCCP-FH code and its input datasets from ISCCP-H.

4 Comparison of four TOA CRK datasets in evaluating FH CRKs.

As mentioned above, there are so far only TOA CRK datasets available in publication. To have a meaningful evaluation for the FH's TOA CRKs by direct comparison, we require a selected TOA CRK dataset to have a similar τ-CTP histogram for at least 12 monthly means for both SW and LW with global coverage. There seems only a very limited number of such datasets that satisfy the requirement and we have found only three other qualified TOA CRK datasets: (1) the one used in Z2012, shortened as 'MZ' (for Model-mean climate states based by Zelinka), (2) the one used in Zhou et al. (2013), whose mean state is from the European Centre for Medium-Range Weather Forecasts (ECMWF) Interim Re-Analysis (ERA-Interim) assimilation, shortened as 'OZ' (for semi-Observation-based produced by Zelinka), and (3) the initial release

of the CERES FluxByCldTyp-Day/Month Ed4A products, shortened as 'CS' (Sun et al., 2019; CERES Science Team, 2020). The FluxByCldTyp is one of the categories of the CERES Single Scanner Footprint (SSF) 1deg Level-3 products.

Table 1 shows the basic characteristics of the four TOA CRK datasets from FH, CS, MZ and OZ. Both the MZ and OZ CRKs are zonal, monthly means in their original form, produced using the same Fu-Liou radiation code, but with different (zonal) mean climate states as input. In their CRK calculation, single-layer clouds are inserted into the atmospheric column of the Fu-Liou radiative transfer model by setting liquid or ice water content to nonzero values at the level closest to the specified CTP for the cloud layer. Their LW and SW CRKs have values for all 49 bins. Their LW CRK may be directly replicated to all longitudes of a global map (i.e., independent of longitudes) but their SW CRK is also function of surface clear-sky albedo and must be mapped to a 2D global map using a surface clear-sky albedo map. For simplicity, we use the FH's surface clear-sky albedo for the mapping because it only makes minor differences if using the CERES' (or others) surface clear-albedo (Appendix B, Zelinka et al., 2012).

The CERES FluxByCldTyp products provide Terra and Aqua daytime 1°-regional gridded daily and monthly averaged TOA radiative fluxes and the associated Moderate Resolution Imaging Spectroradiometer (MODIS) derived cloud properties stratified by cloud optical depth and cloud effective pressure. The FluxByCldTyp products utilize only daytime (solar zenith angle < 82°) observations. The products provide overcast fluxes for 42 cloud types demarcated by 6 cloud optical depth and 7 cloud effective pressure layer bins, and clear-sky flux (in Wm^{-2}). The difference between overcast and clear-sky fluxes is OCRE; when it is divided by 100, it becomes CRK (in $Wm^{-2}\,\%^{-1}$) (Figure 3). This process is exactly the same way as we produce the FH CRKs except the CERES' fluxes are directly provided. Their first τ-bin (of 0 –

1.27) covers the first 2 τ bins (0 – 0.3 – 1.27) of the 7 τ bins in all the other 3 CRK datasets because the CERES-MODIS cloud algorithm can effectively retrieve only the optical depths greater than 0.3. However, we have found that the CS CRKs' first bin indeed has a minimum τ ≈ 0. 05 reported in the CS' monthly mean τ data (for 42 cloud types). In addition, the algorithm has an optical depth detection limit of ≤ 150. The FluxByCldTyp products also treat both the single-layer and multi-layer portions of the upper-level cloud as the upper layer cloud (i.e., including overlapped clouds), in contrast to all the other 3 datasets based on single-layer clouds. The uncertainties for FluxByCldTyp products are not available, but the uncertainty for monthly 1°x1° regional 42 cloud-type and clear-sky SW and LW fluxes are expected to be > 6.2 Wm^{-2} and > 2.6 Wm^{-2}, respectively, based on several uncertainty causes (CERES Science Team, 2020). Note that the effective CTP is used in the FluxByCldTyp production while the physical CTP is used in the calculation for all the other 3 CRK datasets.

To compare TOA CRKs for FH and the other 3 datasets on common ground, we make them have a common spatial resolution of 250-km equal-area map by re-gridding if necessary (Table 1). There are a total of 8252 grid cells on a full 250-km equal-area global map. Typically, the FH CRKs are virtually fully-mapped (only limited by highlands where low/middle cloud types cannot possibly exist as their CTPs may become underground). The longitudinally mapped MZ and OZ CRKs have values for 100% cells for all the 49 bins for LW, but ~97% for SW or Net (because FH's surface clear-sky albedo dataset has no data for polar nights in the SW mapping), implying that there may appear some unrealistic bins below ground level. The CS CRKs have only ~65% cells (of 42 bins) with data, under-sampled by ~1/3, but it is with real topography as FH. The reasons may lie in that some of the 42 cloud types may rarely or never be

present in some regions, and that CERES uses more restrictive procedures to retrieve cloud types for FluxByCldTyp products (CERES Team, 2020).

Figure 3 shows global, annual mean TOA CRKs for 49-bin (42-bin for CS) histogram for MZ, OZ and CS, respectively. With Figure1's left column for the FH's TOA CRKs, we can see that the 4 sets of TOA CRK are similar and they generally have all the features described in Section 3.

Figure 3.

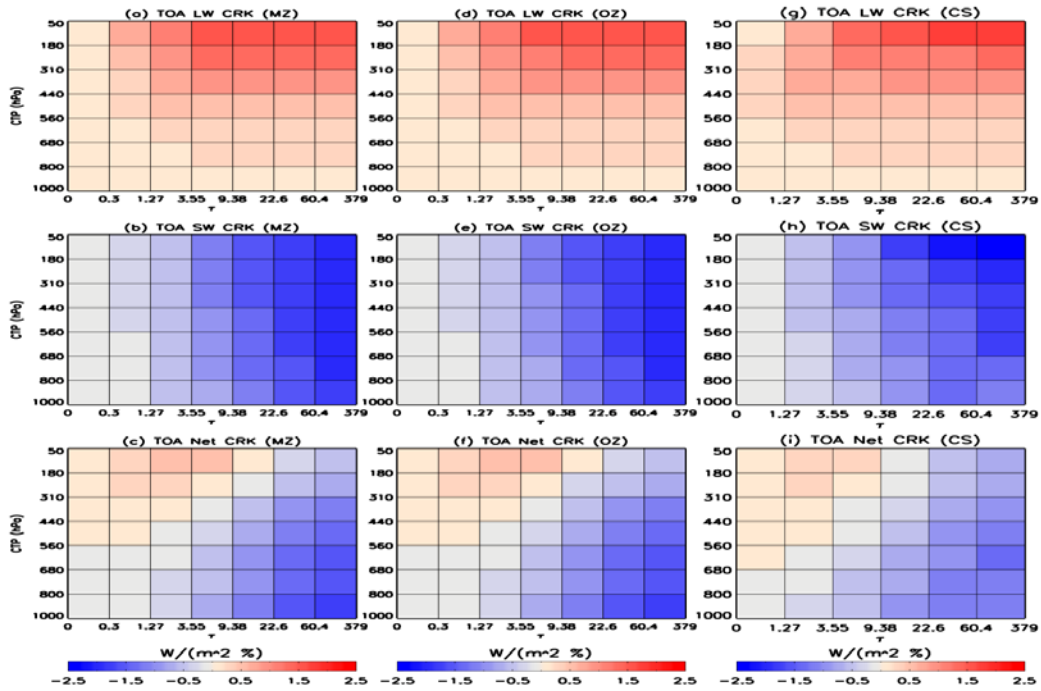

Figure 3. Global, annual mean TOA cloud radiative kernels for 49-bin histogram (42 bins for CS) in Wm^{-2} $\%^{-1}$: (left to right) columns are for MZ, OZ and CS CRKs, respectively, and (top to bottom) rows are for LW, SW and Net CRKs, respectively.

To have a quantitative evaluation for FH and (in general) estimate uncertainties based on all the 4 sets for TOA CRKs, we make a statistical comparison for each of the 6 pairs that are all the possible combinations of the 4 sets as shown in Table 2. From Table 2, we see that all the pairs have a high correlation (> 0.92), with an average of 0.96, 0.99 and 0.97 for LW, SW and Net, respectively. We also see much smaller mean differences (≤ 0.08) and standard deviation (Stdv ≤ 0.027) with the highest correlation (≥ 0.999) between the MZ and OZ CRKs, indicating that the 2 CRKs have relatively high similarities as they are calculated using the same single-layer cloud specification and Fu-Liou code (even though their mean climate states are different) and that CRKs are less sensitive to mean climate states as long as they are reasonably representative. As we are not sure which of the 4 sets represents 'absolute truth', we treat them as ensemble realizations of actual climate such that their differences represent an estimate of the uncertainty in their measurements or datasets (Zhang et al., 2006) without particular favor by using the modulus (absolute) mean difference (e.g., Reynolds, 1988). The modulus mean difference (Stdv) of the 6 pairs are 0.027 (0.122), 0.083 (0.130) and 0.064 (0.162) Wm^{-2} $\%^{-1}$ for LW, SW and Net, respectively. Their (bias included) RMS are 0.124, 0.154 and 0.174 Wm^{-2} $\%^{-1}$, which are our uncertainty estimate for monthly, regional (of 250 km, through the rest of text), cloud-type mean TOA CRKs for LW, SW and Net, respectively. As the MZ and OZ CRKs are not completely independent of each other (see above), these uncertainty estimates are probably underestimated. If we remove the OZ CRKs, and make the same comparison but for the rest 3 datasets (FH, MZ and CS) in all their possible 3 combinations (3 pairs), the RMS is increased by~20% (Table S1 in SI), which may be more objective.

To explore more details in their differences, we partition τ to thin (τ < 3.55) and medium-to-thick (shortened as 'med-thick', for τ ≥ 3.55) and CTP to high (50 – 440 hPa), middle (440 –

680 hPa) and low (680 – 1000 hPa) clouds, and then make zonal means for each of the 6 sub-histograms for LW, SW and Net for FH, CS, MZ and OZ, respectively. To have a physically meaningful comparison, we strictly require that all the data cells of the 4 CRK datasets are matched for all the bins on 250-km equal-area map. For a 7 x 7 histogram, its first two τ bins are required to have data in matching CS' first τ bin. Figure 4a shows the comparison for zonal, annual means for high, middle and low clouds for LW, SW and Net, respectively, for thin-τ, and Figure 4b is the same but for med-thick τ.

Figure 4a

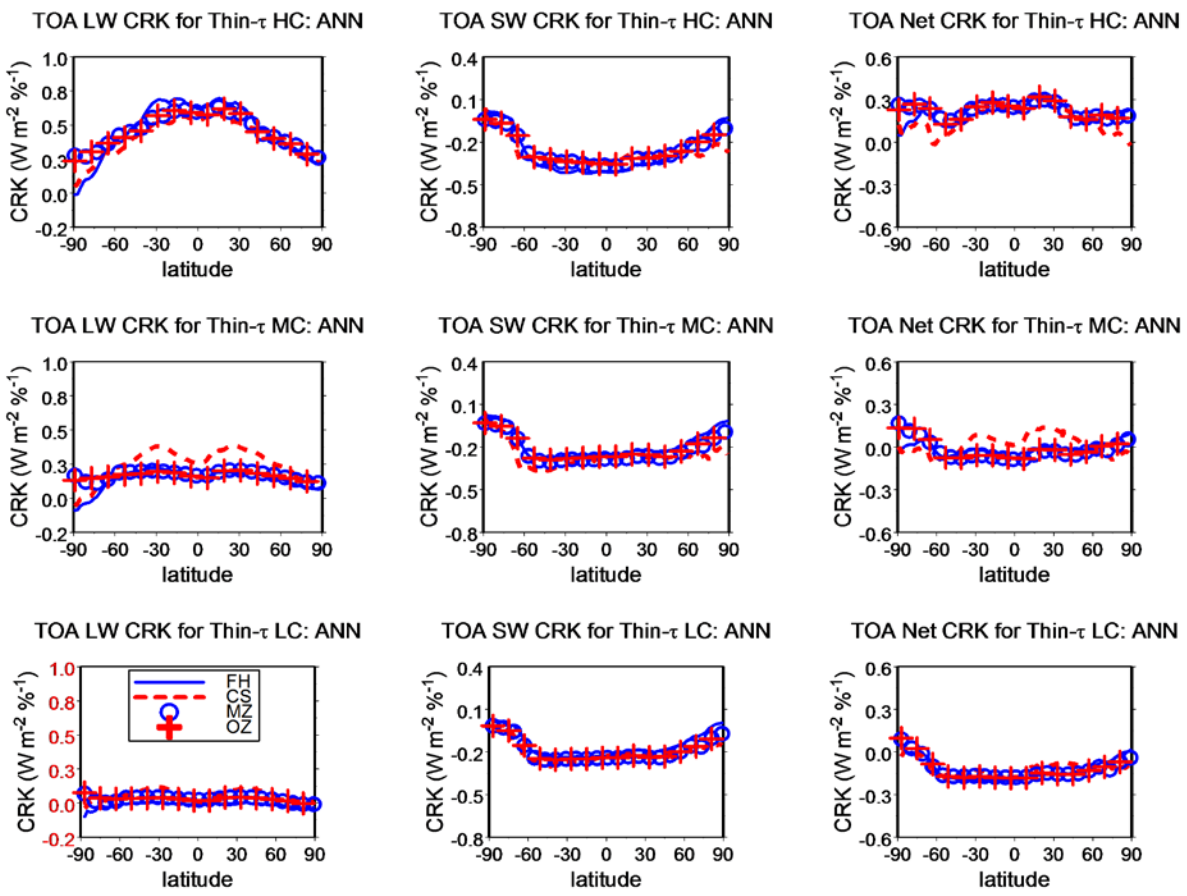

Figure 4a. Comparison of zonal, annual mean TOA cloud radiative kernels for thin τ (< 3.55) for FH, CS, MZ and OZ, respectively, for (top to bottom) high clouds (HC), middle clouds (MC) and low clouds (LC) and (left to right) LW, SW and Net, respectively.

Figure 4b.

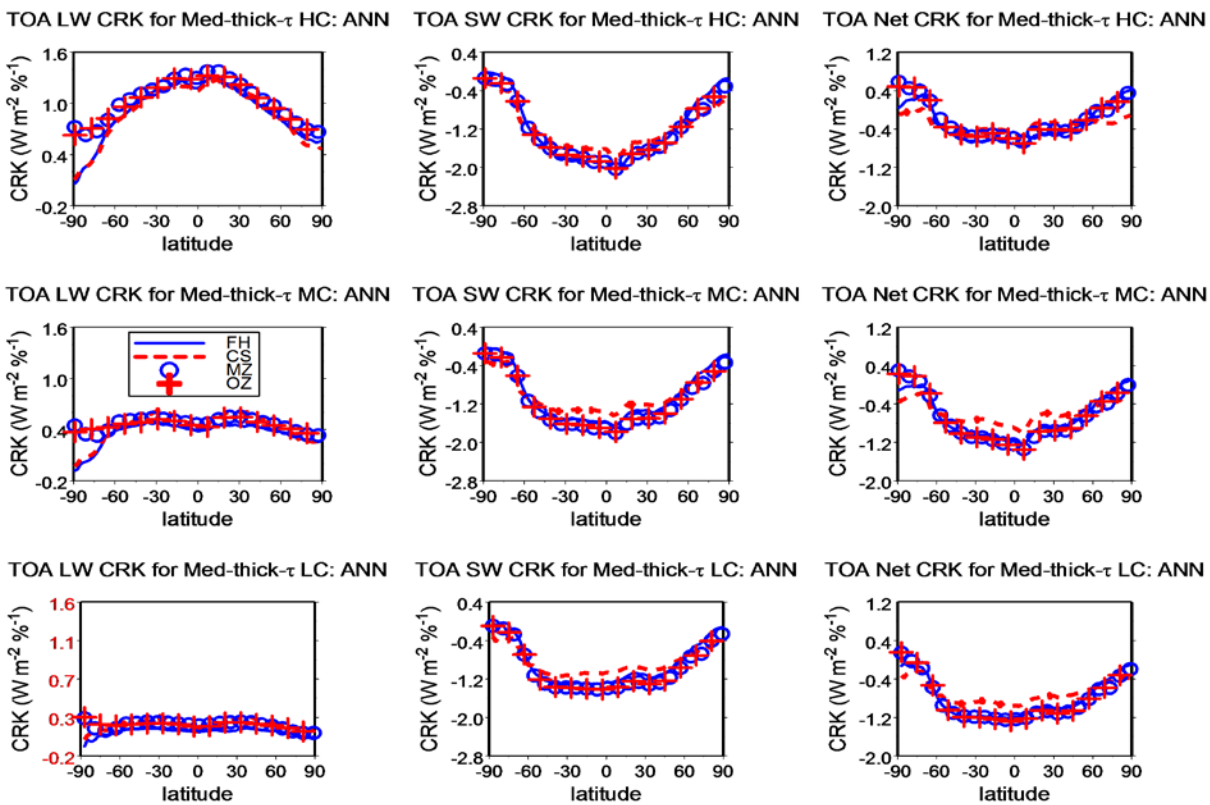

Figure 4b. Same as Figure 4a, but for medium-to-thick ('Med-thick') τ (≥ 3.55) clouds.

Both Figures 4a and 4b show that the 4 TOA CRK sets have a good agreement and their differences are generally within their uncertainty ranges, especially for SW in Figure 4a. The LW CRKs have relatively larger zonal variations for high clouds than middle and low clouds that are relatively flat with the magnitude reduced substantially from high to low clouds, which is likely caused by relatively larger latitudinal variations in cloud top temperature and water vapor

content for high clouds and CTP's dominant role. The mean magnitudes are roughly doubled from thin-τ to med-thick-τ. In contrasts to LW CRKs, the SW CRKs have similar zonal variations with magnitudes (in negative) slightly reduced from high to low clouds (as column τ is dominant). For SW CRK, the mean magnitudes of med-thick-τ (in negative) are about quintuple of that of thin-τ, much larger than LW CRKs' counterparts.

However, three local zonal areas appear to have large differences, exceeding the monthly, regional, and cloud-type mean uncertainty ranges (Table 2). First, over the south polar zones (poleward of ~75° S) , the LW CRKs of FH and CS are nearly coincident for both the thin τ and med-thick τ (Figures 4a and 4b) for all the high, middle and low clouds with magnitude lower than that of MZ and OZ which are also nearly coincident. The magnitude of the differences between the two pairs (FH/CS and MZ/OZ) varies with CTP and zone: decreases from high to low clouds and increases towards the South Pole. The maximum appears at the South Pole, which can be as large as ~0.2 Wm^{-2} $\%^{-1}$ for thin τ and ~0.5 Wm^{-2} $\%^{-1}$, for med-thick τ, about double and quadruple of the RMS (0.124 Wm^{-2} $\%^{-1}$), respectively. Such differences between the two pairs may reflect the different natures between model-based and observation-based CRKs over Antarctic regions, where both models and observations have large uncertainties. They also reflect the difference in temperature/humidity profiles between FH/CS and MZ/OZ since SW CRKs have no such differences in the Antarctic zones. The comparison of temperature profile between ERA-Interim and nnHIRS shows that the former's temperature profile is about 1 – 3 K larger than nnHIRS for 90° S to 60° S zonal average for January (Rossow et al., 2021), which may indicate its contribution to lower FH clear-sky OLR and therefore lower LW CRKs (since TOA LW CRK = clear-sky minus overcast OLR). In addition, CS uses observed clear-sky OLR, which is likely with lower temperature and drier atmosphere (with respect to overcast) to

contribute to lower clear-sky OLR and LW CRKs. These may partly explain the large differences over the Antarctic areas between the two pairs. Second, over the subtropical latitudes around 30° for both the hemispheres, there appear up to 0.2 Wm^{-2} $\%^{-1}$ differences (nearly double the RMS) between CS and all the other 3 sets, but only for the thin-τ and middle clouds of LW CRK (Figure 4a). As the subtropical zones are where cloudiness reaches minima (Peixoto and Oort, 1991), it is difficult for MODIS-CERES to have accurate retrievals when both of small cloud amount and thin τ (< 3.6) are present that may explain the wave-like outlies from CS. We have looked at the corresponding CS' zonal-mean cloud fraction (not shown) in the same fashion as Figures 4a and 4b (high, middle and low clouds for the two τ ranges), which shows that the cloud fraction over the said subtropical latitudes for middle clouds and thin-τ is very low, $\lesssim$ 1%, while all the others are generally larger than 1% (except middle clouds with med-thick τ, for which it may become better for retrievals because of thicker τ). In addition, for these zonal areas, the effective CTP used by CS may also contribute to the differences, especially for cirrus clouds. Third, over the tropical and subtropical zones (~45° S to ~45° N), the CS' SW CRKs for med-thick τ (Figure 4b), mainly for middle and low clouds, are larger than the other 3 sets with the difference of up to 0.4 Wm^{-2} $\%^{-1}$ around the equator, more than double of the SW CRK's RMS (0.154). After some investigation (e.g., overlapping cloud effects), we are unable to attribute such differences to any single cause. However, note that the peak of the difference appears in the equatorial belt of strong convections around the Intertropical Convection Zone (ITCZ) areas that may make it difficult for MODIS-CERES to have accurate retrievals for low and middle clouds.

In short, the FH TOA CRKs agree reasonably well with the other three CRK datasets and all the four datasets of TOA cloud radiative kernels perform well. However, there are also a few local zonal areas with relatively large differences of up to double of their RMS in general, and up

to quadruple of the RMS in the extreme for the zones near the South Pole for LW CRKs where both the calculated and observed CRKs have large uncertainties.

5 Uncertainty budget of CRK-derived cloud feedback.

For evaluation on the FH CRKs using CRK-derived cloud feedback results, we use the ISCCP-simulated CFC results from 10 CFMIP1 models (Table 3), which are among the 11 models used in Z2012, but we drop one model because it has a quality issue (personal communication with Dr. Zelinka). We use the 10 CFMIP models' results because they are the best fit to our evaluation for direct comparison and we cannot find more relevant results from modern CMIP6/CFMIP3 results pertinent to our present purpose.

In the same fashion as done for CRK (Table 2), we have compared CFC from control run (1 x CO_2) to 2 x CO_2 (equilibrium) run for a total of 45 pairs of all the possible combinations for the 10 CFMIP1 models (normalized by surface air temperature). The modulus mean of the 45 pairs' mean difference (Stdv) is 0.004 (0.332) in $\%K^{-1}$, translated to RMS of 0.332 $\%K^{-1}$, which is our uncertainty estimate for monthly, regional, cloud-type mean CFC. For the details, see Table S2 in SI.

Given the uncertainties (RMS) of CRKs (Table 2) and CFC (Table S2 in SI), we can have a quantitative estimate of the uncertainty budget for cloud feedback. The CRK-derived cloud feedback is $K_{x_i}\frac{dX_i}{dT_s}$ (Section 1) with X_i for cloud amount. For simplicity, we rewrite it as $k{\cdot}\Delta C$, where k is our CRK ($=K_{x_i}$) that can be for LW, SW or Net, and ΔC is CFC ($=\frac{dX_i}{dT_s}$). Thus, the cloud feedback uncertainty may be estimated by its differential change, which can be

decomposed into two terms with uncertainties (RMS) contributed by CRK and CFC, respectively, as shown in Eq. (3):

$$\delta(k \cdot \Delta C) = \delta k \cdot (\Delta C) + k \cdot \delta(\Delta C) \quad (3)$$

where, the left side term is the total cloud feedback uncertainty, and the two right side terms, $\delta k \cdot (\Delta C)$ and $k \cdot \delta(\Delta C)$, are its decomposed ones, associated with the uncertainties contributed by CRK (k) and CFC (ΔC), respectively. The values of δk and $\delta(\Delta C)$ can be directly taken from their RMS while k and ΔC can be taken from the average of the absolute mean X and Y from Table 2 and Table S2 (in SI), respectively. Table 4 shows the uncertainty budget estimates for cloud feedback based on Eq. (3), indicating that the cloud feedback uncertainty, $\delta(k \cdot \Delta C)$, is 0.177, 0.318 and 0.142 Wm^{-2} K^{-1}, for LW, SW and Net, respectively. Note that the CFC-uncertainty associated term, $k \cdot \delta(\Delta C)$, is 0.176, 0.316 and 0.140 Wm^{-2} K^{-1}, for LW, SW and Net, respectively, which contributes around two-order larger (> 98.5% of the total uncertainty) than the CRK-uncertainty associated term, $\delta k \cdot (\Delta C)$, which is respectively 0.0012, 0.0015 and 0.0017 Wm^{-2} K^{-1}. The uncertainty budget provides statistical support for why cloud radiative kernel's uncertainty is less important compared with spread of GCM CFC uncertainty. The recent CMIP6 experiments show cloud feedback uncertainty of ~0.36 Wm^{-2} K^{-1} (0.49 and 0.26 for SW and LW, respectively) in 1 Stdv, compared with CMIP5's of ~0.34 Wm^{-2} K^{-1} (0.38 and 0.18 for SW and LW, respectively) (Zelinka et al., 2020b). These uncertainty estimates are comparable to ours even though our results are based on the 10 CFMIP1 (CMIP3 era) models.

6 Preliminary TOA, SFC and ATM cloud feedback results derived using FH CRKs.

Based on the ISCCP-simulated cloud fraction change (CFC) from the 10 models, we can calculate cloud feedback at TOA, surface, and in the atmosphere using Eq. (2e) (equivalent to

$K_i \frac{dX_i}{dT_s}$, Section 1). Since the SFC and ATM cloud feedback derived from the SFC and ATM CRKs have not been previously published, we first make our direct comparison of cloud feedback with published results forTOA cloud feedbacks in this section and leave an alternative, direct comparison of short-term cloud feedback to Section 7. We use Z2012's results as they are relatively more comprehensive and relevant (based on the same CFMIP1 models' CFC results, Section 5). However, we also look at some overall characteristics of SFC and ATM cloud feedback in global and zonal means. We emphasize that the SFC and ATM cloud feedback are just the two components decomposed from the TOA cloud feedback as shown in Eq. (2e) (Section 2).

Figure 5.

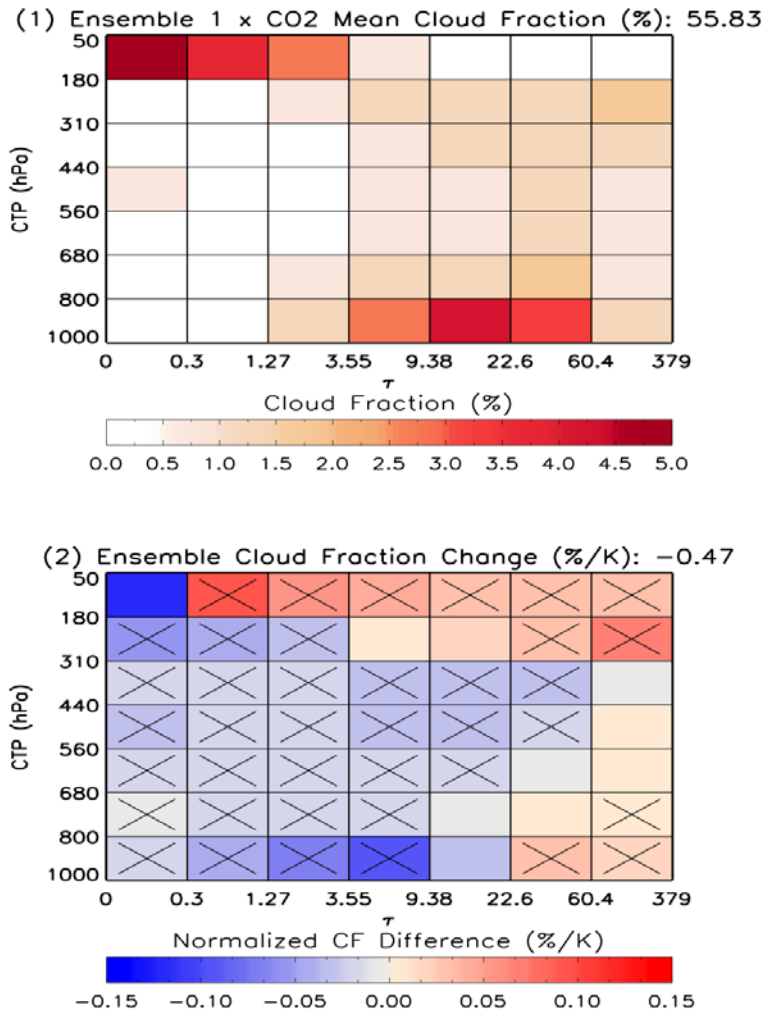

Figure 5. Global, annual, 10 CFMIP1 model ensemble mean cloud fraction for 1 x CO_2 in (1), and cloud fraction changes from 2 x CO_2 runs in (2) with respect to (1), normalized by the change of each model's global mean surface air temperature changes between the two states in % K^{-1}. A bin marked by 'x' indicates that ≥ 80% of models agree on the sign of the bin. The sum of the 49 bins is shown in each title.

Figure 5 shows global, annual and 10-model ensemble mean cloud fraction for 1 x CO_2 and CFC from 2 x CO_2 experiments. They are very close to Z2012's panels (a) and (c) of their Figure 2 with slightly different total value (sum of 49 bins, shown in the titles) though we only use 10 of 11 of their models' data. In the lower panel, we also show cross signs ('x') for the bins with ≥ 80% of models having the same sign, which are identical to the Z2012's sign indicators (but theirs are for ≥ 75% of the 11 models). The CFC with large magnitude mainly appears in high clouds (CTP < 440 hPa) and near-surface clouds (CTP > 800 hPa). Most of the CFCs are negative (decrease of cloud amount) with the largest (in magnitude) of -0.12 $\%K^{-1}$, about 1/4 of the total (-0.47 $\%K^{-1}$), for CTP < 180 and thinnest τ ($\tau \leq 0.3$), but there also appear large positive bins in high clouds (CTP < 310) and near-surface clouds with thick τ (> 22.6). The CFC features are consistent with that double CO_2 experiments generally cause high clouds to shift upward and low clouds with thin-medium τ reduced.

Figure 6 shows the cloud feedback histograms for global and annual ensemble mean based on the 10 models for (left to right) TOA, SFC and ATM and (top to bottom) LW, SW and Net cloud feedback. The TOA cloud feedback panels are highly similar to Z2012's (d), (e) and (f) of their Figure2 (although our cloud feedback results are from completely independent FH CRKs with only 10 of their 11 CFMIP1 models used). The cross signs ('x') in the left column (with the same meaning as Figure 5) agree with Z2012's with slight differences. Table 5 shows the range of the total cloud feedback for global and annual mean for LW, SW and Net at TOA, surface, and in the atmosphere along with their ensemble values. All the ranges between Table 5 and Z2012 are consistent. Note that Table 5 also tells that the model spread is large.

Figure 6.

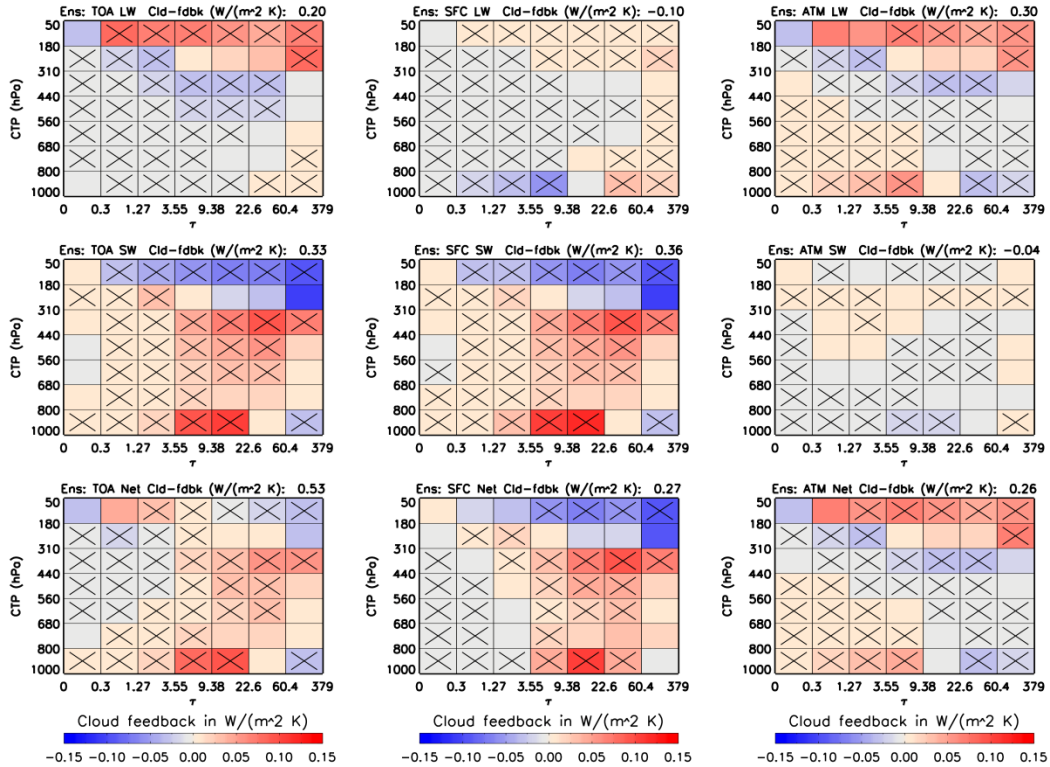

Figure 6. Global, annual, ensemble ('Ens') cloud feedback for (left to right) TOA, surface and atmosphere for (top to bottom) LW, SW and Net, respectively. They are obtained by multiplying the (normalized) cloud fraction changes with FH CRKs for each bin, 250-km equal-area cell and month, and then average to the global, annual, ensemble mean. A bin marked by 'x' indicates that ≥ 80% of models agree on the sign of the bin. The sum of the 49 bins is shown in each title.

The (top middle) SFC LW cloud feedback of Figure 6 shows that the majority of bins are negative with large-magnitude appearing in low clouds (1000 ⩾ CTP > 800) among the thin and medium τ range. The near-surface clouds with thick τ, all bins with τ ≥ 60.4 and the majority of clouds with CTP < 310 are positive with several bins in large magnitude. Overall, the SFC LW cloud feedback has net cooling effects of -0.10 Wm^{-2} K^{-1}, about half of the TOA LW's (in

magnitude). The SFC SW cloud feedback is similar to the TOA's (because their SW CRKs are similar, Section 3) with total feedback of 0.36 versus TOA's 0.33 Wm^{-2} K^{-1}. As the sum of the SFC LW's and SW's cloud feedback with the latter's dominance, the SFC Net cloud feedback shows that most of the high clouds (CTP < 310) have large cooling effects and the rest with medium and thick τ have larger heating effects on the surface that makes the total cloud feedback equal to 0.27 Wm^{-2} K^{-1}, about half of TOA Net's.

As the difference between TOA and SFC, large magnitude of the ATM LW cloud feedback mainly appears in high clouds and near-surface clouds. Overall heating is dominant so the total cloud feedback is 0.30 Wm^{-2} K^{-1}, although negative bins appear in nearly half of all bins. The magnitude of the total ATM LW feedback (0.30) is equal to the sum of the magnitude of TOA (0.20) and SFC (-0.10) because both the increase of TOA cloud feedback and the decrease of SFC cloud feedback strengthen the ATM cloud feedback, which results in the cloud feedback of LW ATM being the largest of the three LW's feedback that may play an important role in modulating atmospheric circulation (see below with Figure 8). The small ATM SW cloud feedback with a total of -0.04 Wm^{-2} K^{-1}, one order smaller than all the other (TOA, SFC and ATM) cloud feedbacks in magnitude, is mainly due to small ATM SW CRK. Because the majority of the ATM SW CRK bins are positive and the majority of CFC bins are negative, their product results in the majority (~2/3) of bins with a negative sign. The SW ATM cloud feedback seems the least important of all the cloud feedbacks. As the sum of the ATM LW and SW cloud feedback, the ATM Net cloud feedback is overweighed by LW's since SW's is so small that the ATM Net cloud feedback is like a weak duplication of ATM LW feedback. The total Net feedback of ATM (0.26) is about half of the TOA's (0.53) with another half shared by the SFC's (0.27).

Figure 7 shows the total cloud feedback (of 49 bins) for annual and ensemble mean on the global map for (left to right) TOA, SFC and ATM for (top to bottom) LW, SW and Net, respectively, based on CFCs from 4 models using the FH CRKs. All the LW, SW and Net cloud feedback features in the (left) TOA column are very similar to the left column of Figure 5 in Z2012, though Z2012 uses 5 models, of which we dropped one because of a quality issue (personal communication with Dr. Zelinka). From Figure 7, we can find some interesting features: (1) For LW cloud feedback, almost all the TOA's major features appear in the ATM LW cloud feedback (with the largest global mean for LW) except for both the polar regions where large surface heating appear in the SFC LW cloud feedback with much larger magnitude than both TOA and ATM LW feedback; (2) Although the global mean of the ATM SW cloud feedback is one order smaller than all the other cloud feedback's, the ATM SW has relatively large heating effects in the atmosphere over polar regions while the SFC SW cloud feedback causes heating in the Amazon areas but cooling in the ~60° S belt; (3) For Net cloud feedback, the most noticeable is that the atmosphere of the ITCZ gets heating but that of the South Pacific Convergence Zone (SPCZ) gets cooling while the surface of the Amazon and the SPCZ gets heating but the ~60° belt gets cooling.

Figure 7.

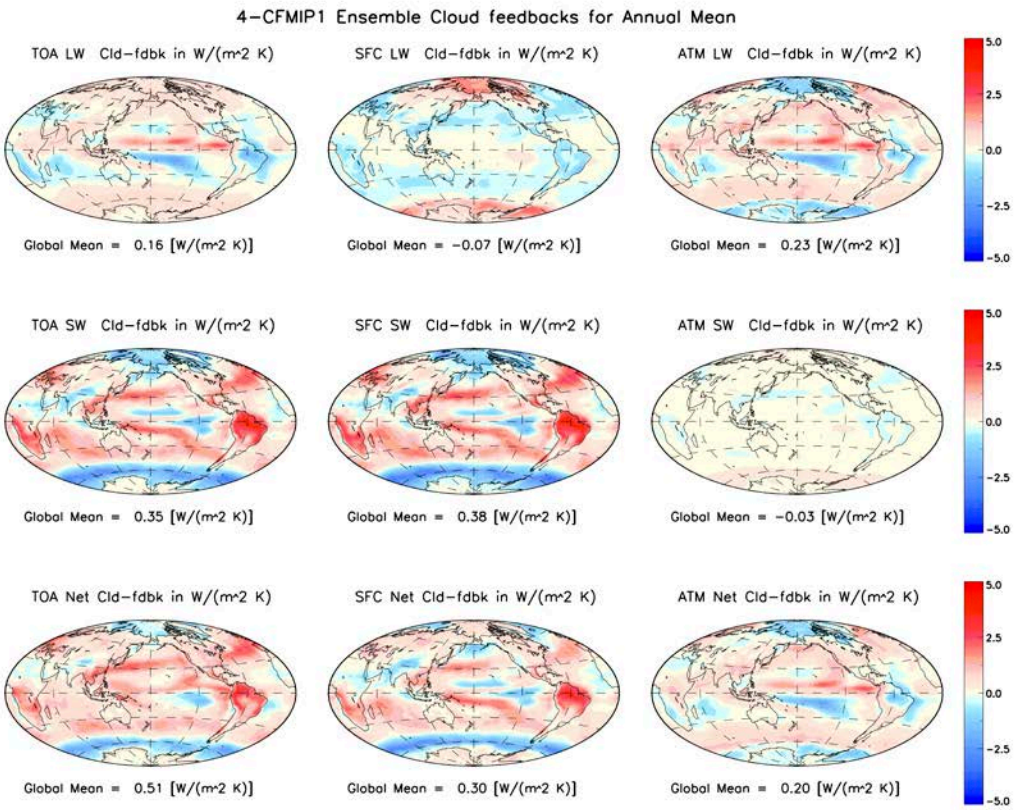

Figure 7. Estimates of the annual and 4-CFMIP1 ensemble mean cloud feedback for (left to right) TOA, SFC and ATM and (top to bottom) LW, SW and Net, respectively, derived using the FH CRKs. The left column is the same as the left column in Z2012's Figure 5, which uses 5 CFMIP1 models: HadSM4, HadSM3, HadGSM1, MICRO (lowres) and AGCM4.0, of which the last is not used here because of a quality issue (see footnotes in Table 3).

Figure 8 shows zonal, (10-model) ensemble mean cloud feedback, partitioned into high, middle and low clouds for (left to right) TOA, SFC and in ATM for (top to bottom) LW, SW and Net, respectively. The upper part of Table 6 shows their respective global mean contributions. The left column for the TOA cloud feedback seems like a duplication of the Figure 6 in Z2012 (but only for 75° S to 75° N), even derived with the completely independent FH CRKs using

only 10 of their 11 models. From the SFC and ATM feedbacks together with the TOA's, we can see some interesting features that may not appear in the TOA-alone feedback. First, Z2012 states that low cloud changes are irrelevant at all latitudes for the TOA LW cloud feedback as the low cloud feedback is nearly zero over all zones as shown in the (top left) TOA LW panel. However, with the SFC and ATM LW feedback available now, we see that the near-zero low cloud feedback in the TOA LW panel is indeed caused by the nearly entire compensation of the sizeable low cloud feedback between SFC and ATM. This is also reflected in their global average as shown in Table 6: the TOA LW feedback for low clouds is only -0.01 but it is -0.07 and 0.06 Wm^{-2} K^{-1} for SFC and ATM, respectively. Second, in the TOA Net cloud feedback, Z2012 states that because of their largely compensatory effects on the SW and LW cloud feedbacks, high cloud feedback contributes less than low cloud's to the net cloud feedback at all latitudes. With the SFC and ATM Net cloud feedback, we clearly see that the compensatory TOA SW and LW high cloud feedback appear in SFC SW (and Net) and ATM LW (and Net), respectively, meaning that the two components are also largely compensated by the SFC and ATM Net high cloud feedback so it seems small in the TOA Net cloud feedback, which is also reflected in their global average in Table 6. In addition, the ATM LW panel in Figure 8 shows that the heating is largely caused by high cloud feedback over ITCZ and midlatitudes while cooling is largely caused by low cloud feedback over Polar Regions. The meridional gradient of the ATM cloud feedback's differential heating/cooling between midlatitudes and the polar regions (as well as tropics and midlatitudes), largely caused by the ATM LW cloud feedback, seems to have an overall effect to strengthen the role, played by the original CRE's meridional gradient between lower latitudes and polar regions, which may increase the rate of generation of

the mean zonal available potential energy, and eventually, enhance meridional energy transport (Kato et al., 2008).

Figure 8.

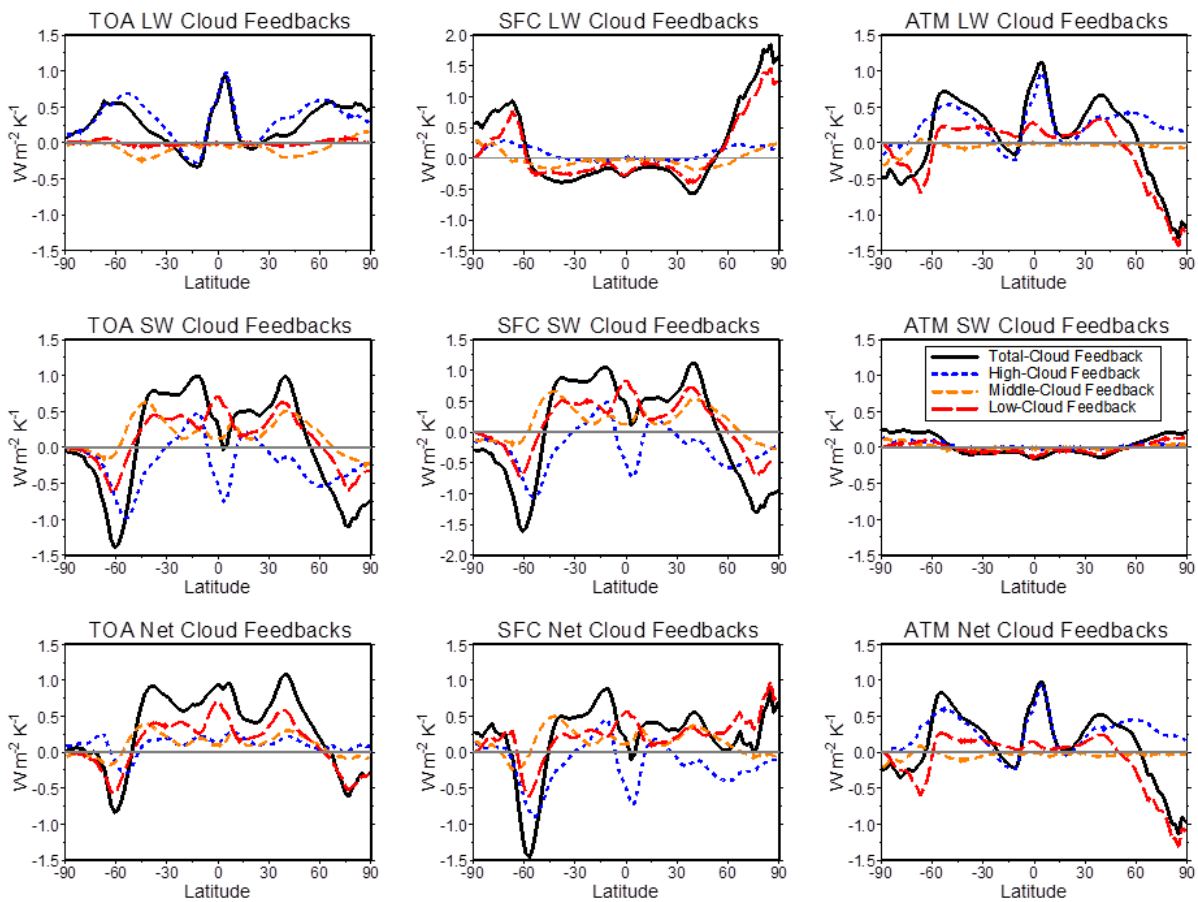

Figure 8. Zonal, annual and (the 10-model) ensemble mean clod feedback, partitioned into high, middle and low clouds with their total for (left to right) TOA, SFC and ATM for (top to bottom) LW, SW and Net, respectively.

Figure 9 is the same as Figure 8 but the cloud feedback is partitioned into contributions from thin-, median- and thick-τ CFCs, and their global mean contributions are also shown in (lower part of) Table 6. The left column in Figure 9 is also very similar to Figure 7 in Z2012. We

note that, for the LW cloud feedback, thin- and medium-τ feedback appear small but their SFC and ATM components are actually sizeable and their radiative effects cannot be overlooked, as also indicated in global average (Table 6).

Figure 9.

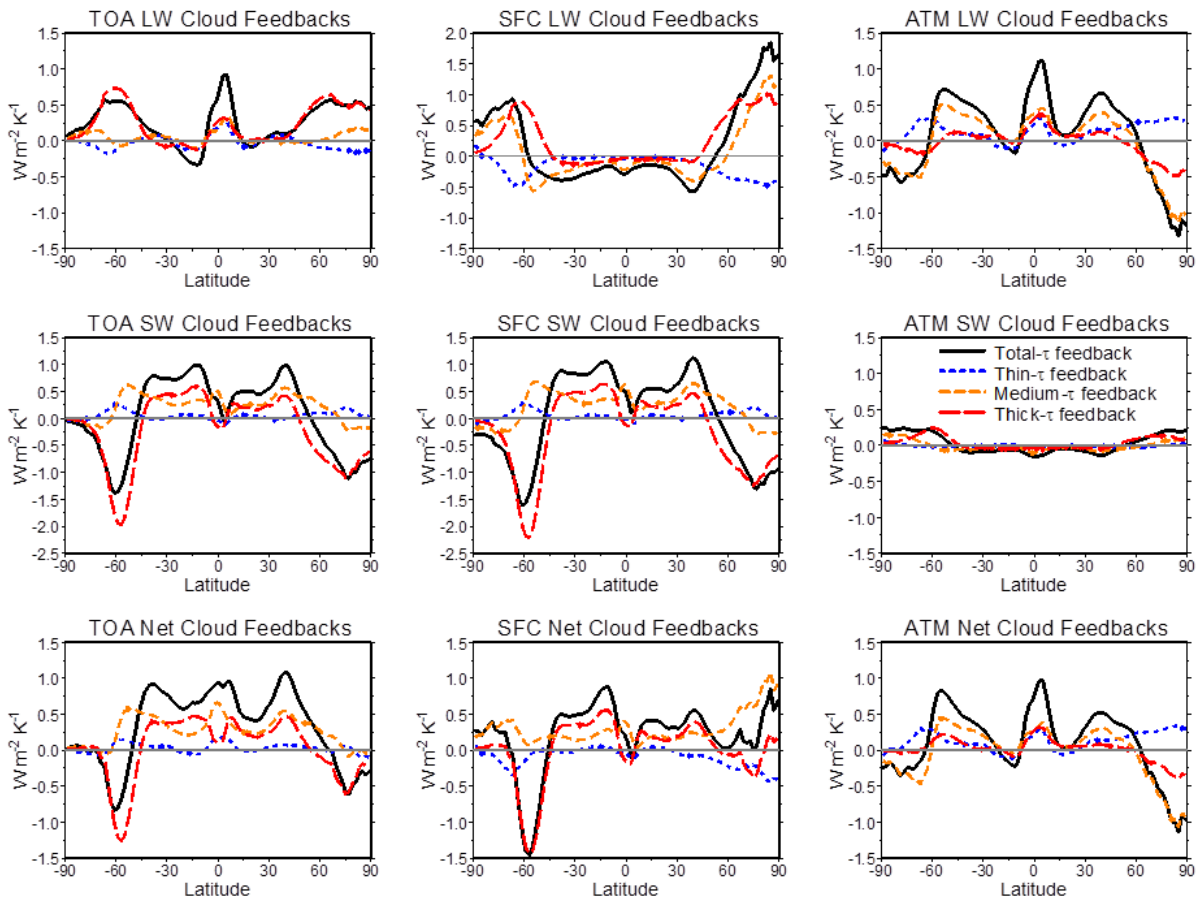

Figure 9. Zonal, annual and (the 10-model) ensemble mean cloud feedback, partitioned into thin, median and thick τ with their total for (left to right) TOA, SFC and ATM for (top to bottom) LW, SW and Net, respectively.

7 Evaluation of cloud radiative kernels and their derived cloud feedback using CERES products.

To justify the linearity for the decomposition of cloud radiative kernels and cloud feedback into the separate earth (SFC) and atmospheric (ATM) systems (from the whole earth-atmosphere system) based on 49 (or 42) cloud types, we conduct two tests. The tests are to investigate (I) whether the ISCCP-FH SFC and ATM CRKs can be used to derive SFC and ATM CREs that agree with observations and (II) whether the FH SFC and ATM CRK-derived cloud feedback has linearity with global mean surface air temperature changes or whether such derived

cloud feedback (in response to climate variations) agree with the cloud feedback derived from observations. We restrict our tests to global, monthly means and do not go into detail as the validation focuses on the cloud-type-based linearity.

The tests rely on observed datasets, but we have to use computed results when they are not available. For overall consistency, all the datasets are selected from the CERES' Terra-Aqua-MODIS Ed4.1 products except surface air temperature (Ts), which is not available from CERES. They are (1) the observed monthly mean cloud fraction (CF) in 6-τ by 7-CTP histogram from the FluxByCldTyp-Day/Month Ed4A dataset of the Single Scanner Footprint (SSF) Level-3 1deg products, which is based on combined MODIS and CERES observations, (2) the observed TOA fluxes from the SSF Level-3 1deg product, and (3) the computed SFC fluxes from the Synoptic TOA and surface fluxes and clouds (SYN) Level-3 1deg product. We select computed SYN SFC flux datasets because no observed global SFC flux datasets are available to date, and the SSF products do not supply SFC fluxes. Thus, the ATM fluxes are a hybrid of SSF and SYN fluxes. All the CERES datasets are for 10 years (120 months for 2007 – 2016). The datasets of (2) and (3) are used to derive the CERES TOA and SFC CREs, respectively, and their differences are the ATM CRE. All the downloaded CF and derived CREs are regridded to our standard 2.5° x 2.0° map from their original 1° x 1° map.

To validate the ISCCP-FH cloud kernels (Test I), we merge the (thinnest) first and second τ to form 6 τ by 7 CTP histogram for our CRKs (by averaging) to be consistent with the CERES CF's (6 x 7) histogram and then calculate the FH CRK-derived CREs for each grid box using $\sum_{i=1}^{42} CRK_i \times CF_i$, where the summation is over all the 42 cloud types. We then compare the calculated (FH) CREs with the CERES' CREs for the 10-year, monthly, global mean time series. Note that, however, as CF is generally not infinitesimal, the above calculation may violate the

rule by which the CRK is designed, which is that the CRK is only applicable to infinitesimal cloud amount changes. Nevertheless, we still go with the test to see how much our CRKs can bear the violation.

Figure 10

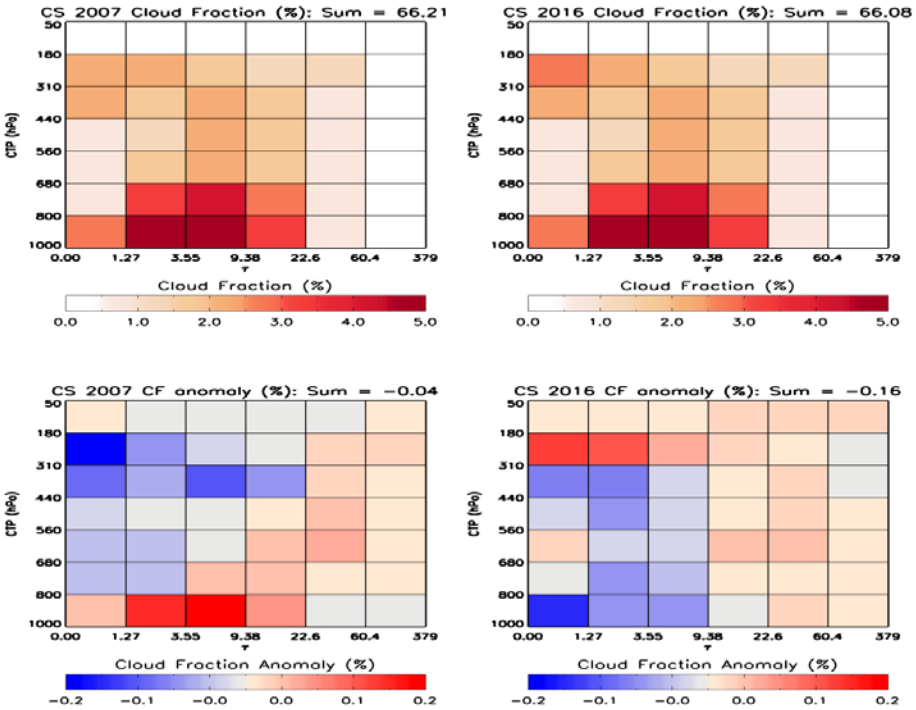

Figure 10. Annual, global mean 6 τ x 7 CTP histogram for cloud fraction (upper panels) and deseasonalized cloud fraction anomaly (lower panels) for (left) 2007 and (right) 2016.

Figure 10's two upper panels are the two examples for annual, global mean 6 τ x 7 CTP histogram for the CERES CF for 2007 and 2016, respectively. Figure 11 shows scatter plots for the nine pairs of CREs from CERES and FH for LW, SW and Net at TOA and SFC, and in ATM, respectively. The CERES and FH CREs have generally good linear relationship with relatively small biases (with respect to 1-to-1 line). Table 7 shows their detailed statistics from the comparison between CERES (X) with FH (Y). The mean correlation of all the 9 pairs is 0.84 with the modulus mean difference (Stdv) of 4.15 (0.79) Wm^{-2}, translated to (bias-included) RMS of 4.22 Wm^{-2}, which is within the known combined uncertainty ranges of the CERES and FH CREs. The lowest correlation (0.431) appears in the SFC LW CRE comparison, indicating that there are relatively large differences in calculating SFC LW CRE for both CERES and FH. The biases are generally less than ~5 W m^{-2} with the largest of 8.30 and 7.24 W m^{-2} for total cloud effects at TOA and SFC, respectively. It is worth noting that compensations between LW and SW for ATM CREs results in the good 1-1 relationship in Net ATM CRE. Moreover, despite the magnitude offset, the TOA results seem to have the best alignment with the 1-1 line, and the ATM shows more deviations from the 1-1 line, which is consistent with our general flux assessment resuts (e.g., Zhang et al., 2021). The statistics are comparable to the comparison results when the real-time-calculated ISCCP-FH flux-derived CREs replace the FH-CRK derived-CREs (not shown) , in which, the mean correlation is 0.79 and the modulus mean difference (Stdv) is 3.58 (1.06) Wm^{-2}, translated to the RMS of 3.73 Wm^{-2}, slightly better than the original comparison. If we use the SYN (instead of SSF) TOA CREs, the mean correlation is 0.78 and modulus mean difference (Stdv) is 4.16 (0.82) Wm^{-2}, translated to the RMS of 4.24 Wm^{-2}, which is is slightly larger (not shown). Therefore, it seems conclusive that the ISCCP-FH CRK-derived CREs are almost as good as the real-time calculated CREs even if only CF is time-

varying in the calculation (i.e., other time-varying atmospheric and surface properties are time invariant so their actual temporal variations are not presented in the CRK CRE calculation) while the CERES SYN based CREs have only small differences with the SSF based CREs (for TOA and part of ATM fluxes). Since the FH CRK-derived and CERES CREs are completely independent datasets, their agreement to within their uncertainty ranges and their linear relationship should be a good validation for both setts of CREs.The good performance of the FH CRK-derived CREs is likely because the magnitude of CF for individual cloud types is not too large (usually ≤ 5%) in the calculation. As a result, our CRKs may be used to estimate CREs when CF histogram datasets are available without heavy flux calculation as usually practised.

Figure 11.

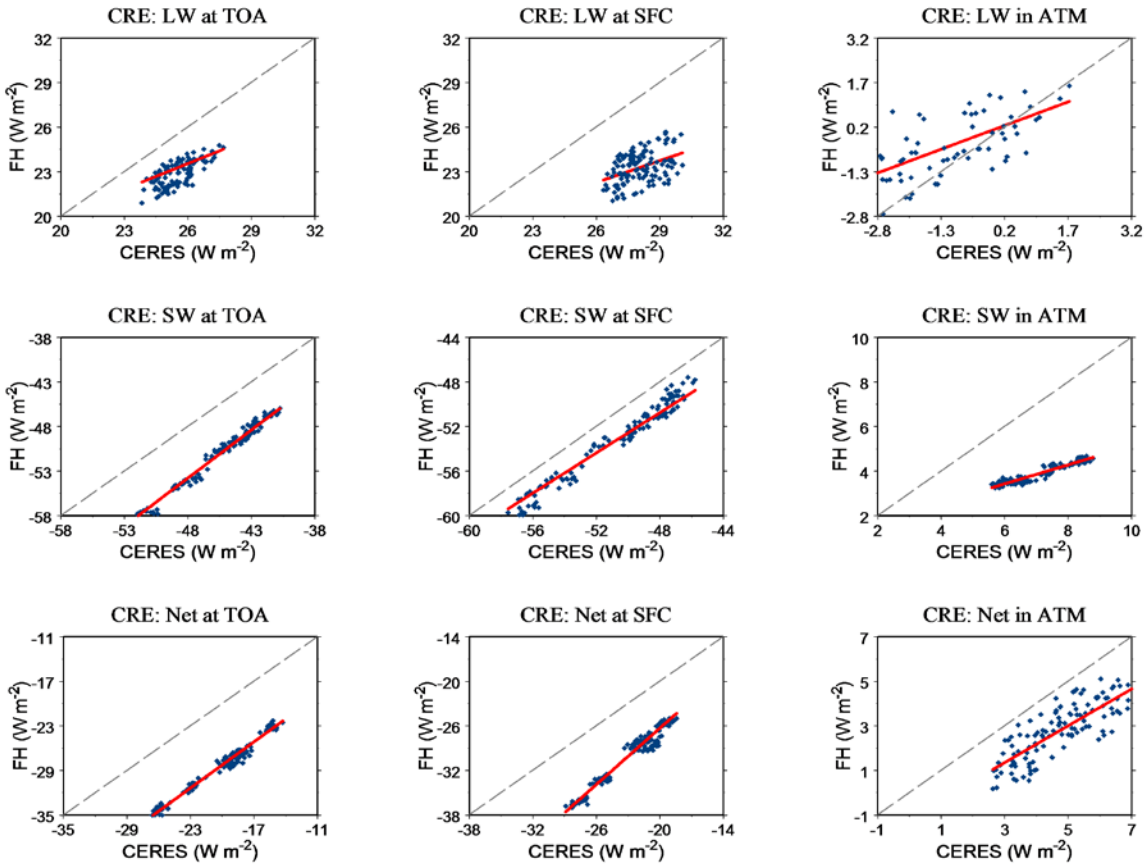

Figure 11. Scatter plots for the comparison between CERES (X) and ISCCP-FH CRK-derived (Y) cloud radiative effects (CRE) in W m^{-2} for global, monthly means of 2007 to 2016. Robust-fit lines are also shown. The X = Y (in dashed) line is also shown for estimating bias.

To conduct the test (II), we first calculate the short-term, climatological variation or anomaly for the datasets. Hence, we deseasonalize all their monthly means of the 10 years to obtain their anomalies, ΔCF and ΔCRE, respectively, from the original CERES CF and CREs. The two lower panels in Figure 10 show the annual, global mean ΔCF on τ-CTP histogram for 2007 and 2016, respectively. We also calculate the anomaly of surface air temperature, ΔT_s, from the GISTEMP data (GISTEMP Team, 2021), which is based on observations and used in global mean. The cloud feedback calculation is based on the formula, $\frac{1}{\Delta Ts}\sum_{i=1}^{42} CRK_i \times \Delta CF_i$ (Eq. 2e, Section2), for FH and $\frac{\Delta CRE}{\Delta Ts}$ for CERES, respectively. We use conventional linear least-squar regression (e.g., Desslr,2010) for anomalous cloud radiative effects, i.e., $\sum_{i=1}^{42} CRK_i \times \Delta CF$ for FH and ΔCRE for CERES, with respect to ΔTs. The slope of the regression line is the strength of the cloud feedback. Positive cloud feedback means that clouds trap additional energy to make the surface warm.

Figure 12 shows the regression results for both CERES and FH for LW, SW and Net at for TOA, SFC and in ATM, respectively. The best agreement appears in SW cloud feedback for all TOA, SFC and ATM, in which CERE and FH have almost coincident regression lines. While they disagree in signs for LW for all TOA, SFC and ATM cloud feedback as well as Net for ATM, FH cloud feedback seems more agreeable with the previous studie as TOA LW cloud

feedback is usually positive (Dessler, 2010 and 2013; Dessler and Loab, 2013). Table 8 shows the cloud feedback values from CERES and FH for LW, SW and Net for TOA, SFC and ATM, respectively, with 95% confidence interval as uncertainty ranges. Both CERES and FH have reasonably good values within the ranges of the previous studies for TOA (short-term) cloud feedback: 0.43 ±0.45, 0.12 ±0.78 and 0.54 ±0.74 W m^{-2} k^{-1} (uncertainty in 2 σ) for LW, SW and Net, respectively, based on ECMWF-CERES (Terra) data from March 2000 to February 2010 (Dessler, 2010) except for CERES' LW feedback that is slightly out of the uncertainty range (with negative sign). For LW (and Net) cloud feedback for SFC and ATM, we can not have a more definitive, quantitative evaluation conclusion. Nevertheless, since all of their slope values are nonzero, their linear relationship with ΔTs seems existent, which gives a positive conclusion for the test (II) although their linear relationship for ATM SW is weak with small slopes due to the largely compensated TOA and SFC SW cloud feedback (Section 6). Although Figure 12 shows disagreements more than agreements, we conclude that theire overall agreement is reasonably good and the test (II) gives an appropriate validation for both the FH and CERES short-term cloud feedback, given that several uncertainty factors contribute to both the datasets, such as the uncertainties of ΔTs, ΔCF and ΔCRE as well as CRKs, and that the two datasets are completely independent. The test (II) may also point out the need to have longer data records because the TOA, SFC and ATM systems may not respond completely on this time scale and to estimate multiple sources of uncertainties as well as their impact on estimating short-term cloud feedback from satellite observations.

Figure 12.

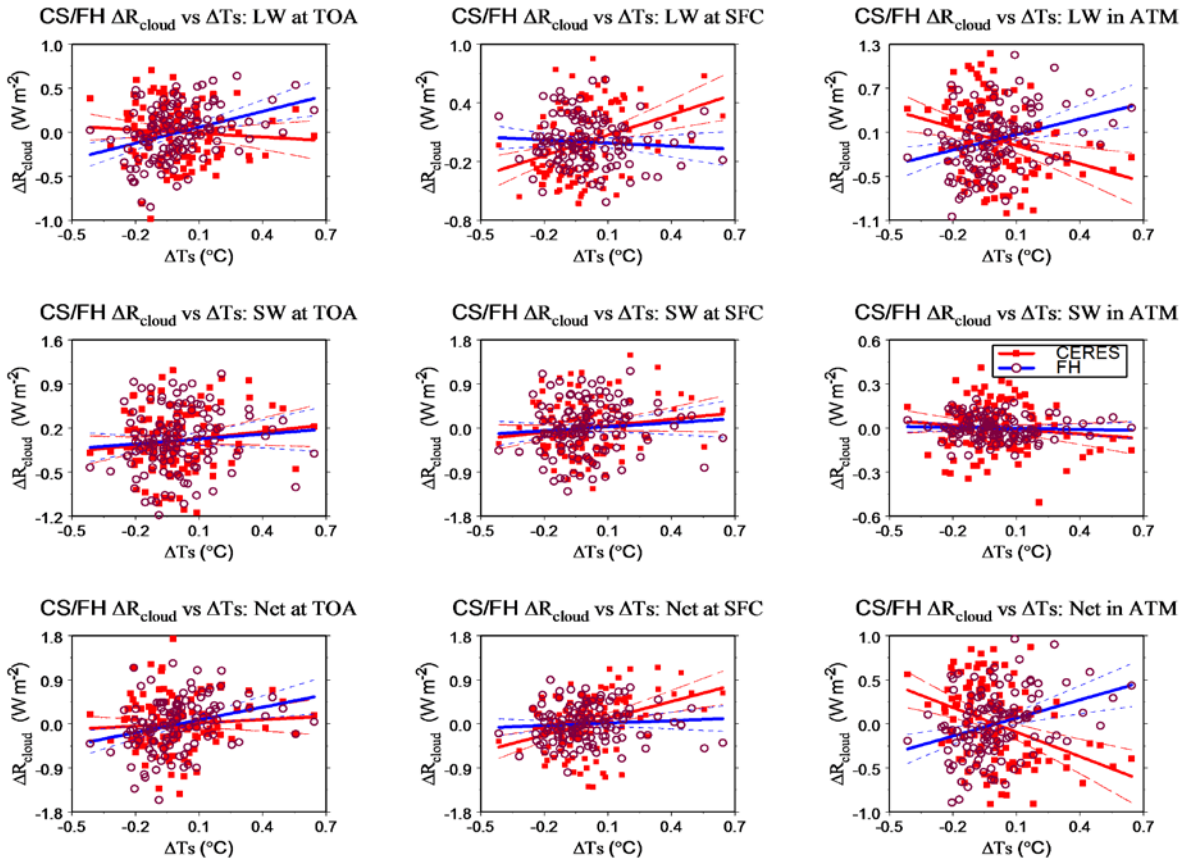

Figure 12. Linear least-square fit for monthly, global mean anomalous CREs (ΔCRE_{cloud}) from CERES (CS) and ISCCP-FH (FH) with respect to anomalous surface air temperature (ΔTs) for years 2007 to 2016 (totally 120 months). All the points and lines with red color are for CERES and blue color for FH. The solid lines are for the regression and dashed lines for the 95% confidence interval.

8 Summary and discussion.

The main purpose of this study is to create observation-based 2D cloud radiative kernels based on the ISCCP-H datasets and obtain the ISCCP-FH CRK-derived cloud feedback at TOA, surface, and in the atmosphere and evaluate them by direct comparison. The direct comparison for CRKs is made with the CRKs from from the other three presentative datasets. The

comparison is also against the ensemble cloud feedback from 10 CFMIP1 models (Z2012's) for TOA cloud feedback (for doubled CO_2 cloud changes) and the cloud feedback derived from CERES products for all TOA, SFC and ATM cloud feedback (for short-term climatological anomalies). In addition, indirect compareson of CREs is used for CRK validation.

With the observation-based ISCCP-H datasets as inputs, we have used the ISCCP-FH profile flux production code to calculate the ISCCP-FH cloud radiative kernels at TOA, surface, and in the atmosphere for SW and LW, and their sum, Net, in 3-hourly on 110-km (and their replicated 250-km) equal-area maps, where the SFC and ATM CRKs are the two components decomposed from the TOA CRK's based on linear operation (Eq. 2d). By design, the FH cloud radiative kernels are as realistic as possible with self-consistency.

The FH TOA, SFC and ATM CRKs for LW, SW and Net (Figures 1 and 2) show physically clear, overall quantitative pictures for 49 individual cloud types. The noticeable features of the CRKs are the CTP-dominant, horizontal-layered structure in all the LW CRKs and the column-τ dominant, vertical-layered structure in SW CRK histograms at TOA and SFC. The TOA and SFC Net CRKs show a roughly antisymmetric structure with respect to their diagonal line (in forward-slash and backslash direction, respectively). As the difference between the TOA and SFC CRKs, the LW and Net ATM CRKs show general heating (cooling) influence by high (low) clouds but only weak effects appear in the SW ATM CRK. The comparison for the 4 TOA CRK datasets, FH, MZ, OZ and CS, shows that the FH CRKs agree reasonably well with the other 3 sets of CRKs, and that, in general, the 4 sets of CRKs perform well and their differences are within their uncertainty ranges. However, in their zonal means, there appear three locally large differences of up to double or so of their RMS, and, in extreme cases, up to quadruple of the RMS for the zones near the South Pole, where both the calculated and observed

CRKs have large uncertainties. Therefore, given their different nature, the 4 sets of the TOA CRKs are more or less comparable in their practical usefulness though CS may somehow suffer under sampling that needs some caution in using it.

Moreover, through the comparison, we have estimated their uncertainties (RMS) as 0.124, 0.154 and 0.174 Wm^{-2} $\%^{-1}$, for LW, SW and Net, respectively, for (250-km) regional, monthly, cloud-type mean TOA CRKs. As the MZ and OZ CRKs are not completely independent of each other, the above uncertainty estimates are probably underestimated. If we remove the OZ CRKs, the RMS is increased by~20%, which may be more objective.

Before calculating CRK-derived cloud feedback, we have also estimated cloud fraction change uncertainty as 0.332 % K^{-1}, based on 45 pairs of all the possible combinations of the 10 CFMIP1 models' ISCCP-simulation for double CO_2 experiments. Combining uncertainties of CRKs and CFC with their means, we have estimated the uncertainty budget for the CRK-derived cloud feedback as 0.177, 0.318 and 0.142 Wm^{-2} K^{-1}, for LW, SW and Net, respectively, to which the CFC-associated uncertainty term contributes around two-order larger than that of the CRK-associated uncertainty term, accounting for > 98.5% of the total uncertainty. The implication is that the priority for improving cloud feedback accuracy is to have more accurate cloud fraction changes while CRKs are relatively accurate enough. Indeed, in viewing all the individual 10 models' CFC's global, annual mean matrixes, we see that they are very diversified (not show) that is also reflected in their ranges of their total global and annual means (Table 5) and their low correlation (of 0.13 in average, Table S2 in SI). The recent CMIP6 experiments show cloud feedback uncertainty of ~0.36 Wm^{-2} K^{-1} (0.49 and 0.26 for SW and LW, respectively) in 1 Stdv, compared with CMIP5's of ~0.34 Wm-^{2} K^{-1} (0.38 and 0.18 for SW and

LW, respectively) (Zelinka et al., 2020b). Both of the uncertainties are comparable with our above uncertainty values even though we use CFMIP1/CMIP3 era data.

We have shown that the cloud feedback derived from the FH's TOA CRKs is highly similar to Z2012's counterparts (Figures 6, 7, 8 and 9 vs. Figures 2, 5, 6 and 7 in Z2012) though we use our completely independent CRKs with one model dropped from their original models used in Z2012. These comparisons may be thought to be an additional validation for the FH's TOA CRKs. In addition, we have conducted two further validation tests for the FH CRKs and their derived cloud feedback for LW, SW and Net at TOA and SFC, and in ATM. The test (I) compared the ISCCP-FH CRK-derived and the CERES' CREs, which shows that the two sets of CREs agree to within their combined uncertainty ranges. The test (II) compared the ISCCP-FH CRK-derived and the CERES' cloud feedback (in response to short-term climate variation). It shows that their linear relationship with ΔTs seems existent and therefore gives a positive conclusion for the test. Given that several uncertainty factors to contribute to both the datasets such as uncertainties of ΔTs, CF (and ΔCF) and CRE (and ΔCRE) as well as CRKs and that the ISCCP-FH and CERES datasets are completely independent, their overall agreement seems to give a good validation for the ISCCP-FH CRKs and their derived cloud feedback as well as the CERES' observed and computed CREs and derived cloud feebback.

We have shown that the cloud-type based decomposition of the TOA CRKs as well as their derived cloud feedback into their SFC and ATM components is mathematically and physically justified based on both the theoretical development (Eqs. 2a, 2b, 2c, 2d and 2e) and the validation studies against available model results (at TOA, Sections 4 and 6) and observational (or calculated if no observation is available) results (Section 7). Thus we have validated the linearity assumption for the CRKs and the CRK-derived cloud feedback over the

cloud-type-based decomposition on atmospheric column and surface (but governed by the overall assumption that no interactions or nonlinear responses among the various climate processes are permitted, Section 1).

In this study, we focus on methodology and evaluation so we do not fully explore possible applications of the SFC and ATM CRKs and their derived cloud feedback. Nevertheless, even with the preliminary results, there have already appeared several possible applications as summarize in the following. (1) One can easily obtain the SFC and ATM cloud radiative effects and cloud feedback using the SFC and ATM CRKs if the ISCCP-simulated cloud fraction and its changes are available from models or observations without relying on time-consuming calculations for CREs (Section 7) and using 'residual' or 'adjust' methods for cloud feedback as used in Kramer et al. (2019). (2) If one wants to explore more details in the conventional (i.e., TOA) cloud feedback and understand how it impacts atmosphere and surface in different ways, the derived, decomposed SFC and ATM cloud feedback must be available. (3) The knowledge of the SFC and ATM cloud feedback helps reveal what maypossibly be significant but appear hidden/insignificant cloud feedback in the TOA-alone feedback, caused by compensation of sizeable SFC and ATM feedback as exemplified in Section 6. The separated, significant SFC and ATM feedback may deepen our understanding of their individual influences on radiation and cloud feedback that is not obvious from the TOA-alone cloud feedback results. (4) To understand dynamic roles of cloud feedback in the atmospheric and oceanic circulation and energy transport, one needs to know specific cloud feedback in the atmosphere and ocean (surface), respectively, which cannot possibly be proceeded with the gross cloud feedback for the earth-atmosphere system (i.e., the TOA-only cloud feedback). As shown in Figure 8, the ATM LW cloud feedback may play a role in enhancing meridional atmospheric energy transport

caused by meridional gradient of the atmospheric cloud radiative effects. (5) The CRK-derived SFC and ATM cloud feedback may also be used to evaluate GCM results as done by Kramer et al. (2019) . We hope to have more detailed exploration of the SFC and ATM CRK-derived cloud feedback using the updated CMIP6 model results in a future study.

APPENDIX A

CRK uncertainty due to dry bias of water vapor under cloud layers

There has been a concern about the effect of dry bias of water vapor when the clear-sky water vapor is used in the cloud-free layers under cloud layers. To investigate this issue, we conduct a sensitivity study to test how much error/uncertainty may be caused in the CRK calculation by such a dry bias. To do so, we have tried to find relatively reliable, global datasets for water vapor variation with cloud covers. However, such datasets are extremely rare and we can only find one relatively good dataset in Gaffen and Elliott (1993). The dataset provides seasonal-mean, surface-to-400-mb column water vapor (W, in kg m^{-2}) under four cloud categories, namely, clear (CLR), scattered (SCT), broken (BKN) and overcast (OVC) with 0%, 31%, 75% and 100% cloud cover, respectively, based on 3-year (daytime) radiosonde and surface cloud observations from 15 Northern Hemisphere stations. The locations of the 15 stations are from the equator to 60° N on land. The differences of W for the cloudy scenes (SCT, BKN and OVC) with W_{clr} represent the amount of column water vapor that should be increased for the cloud layers and the cloud-free layers under the cloud layers. With W for the four cloud categories, we can calculate the dry-bias under SCT, BKN and OVC conditions with respect to clear-sky W, or W_{clr} as follows.

$$C01 = (1 - \frac{W_{sct}}{W_{clr}}) * 100 \quad \text{(A1)}$$

$$C02 = (1 - \frac{W_{bkn}}{W_{clr}}) * 100 \quad \text{(A2)}$$

$$C03 = (1 - \frac{W_{ovc}}{W_{clr}}) * 100 \quad \text{(A3)}$$

where C01, C02 and C03 are the dry-bias-correction ratio (in %) to W_{clr}, function of latitude and season, for SCT, BKN and OVC, respectively, and their sign is usually negative, meaning underestimate of W_{clr} if it is used under cloudy scenes. The dry-bias correction amount can then be obtained by multiplying C01, C02 or C03 by W_{clr} for SCT, BKN or OVC, respectively. Thus, we can add the correction amount to the original column water vapor (before the saturation) in the FH CRK calculation for the assumed scenes (SCT, BKN or OVC), and compare the new CRKs with the original ones to estimate errors from the W changes for the three cloudy scenes. Note that the correction amount is for both the cloud and cloud-free layers under the cloud layers. The FH CRKs have already added water vapors within cloud layers by water vapor saturation (Section 2). The reasons for the cloud layer water vapor saturation are: (1) The nnHIRS' humidity is for clear or near-clear sky so it is dry-biased, (2) The water vapor saturation is a necessary physical condition for clouds to form and it makes the gas absorption/scattering less biased, and (3) The early test for TOVS precipitable water (which also has a dry bias similar to nnHIRS) as described in Zhang et al. (2004) indicates that such a saturation for cloudy conditions compared with clear conditions is consistent with the analysis of radiosonde data by Gaffen and Elliott (1993). Therefore, the net added amount for the sensitivity study for the cloud-free layers (under clouds) is the residual, the difference between the calculated correction amount and the increased amount from the saturation.

Figure A1 shows C01, C02 and C03 for DJF, MAM, JJA and SON, and Figure A2 shows their robust-fitted values only, where the 60° N values are extended to all the 60° N poleward latitudes (since we do not have reliable values for the polar region). The four seasonal values are assumed to represent the values of the 15th of January, April, July and October. They are used to interpolate the values for the other eight months (also for the 15th day of each month). The 1° latitudinal values are interpolated from the robust-fitted values so we have all the northern hemispheric climatology for 12 months, which can be applied to the southern hemisphere with 6-month difference in time between the two hemispheres. This generalization has some risks but we seem to have no other better replacement and, for sensitivity studies, it is probably sufficiently acceptable.

Figure A1.

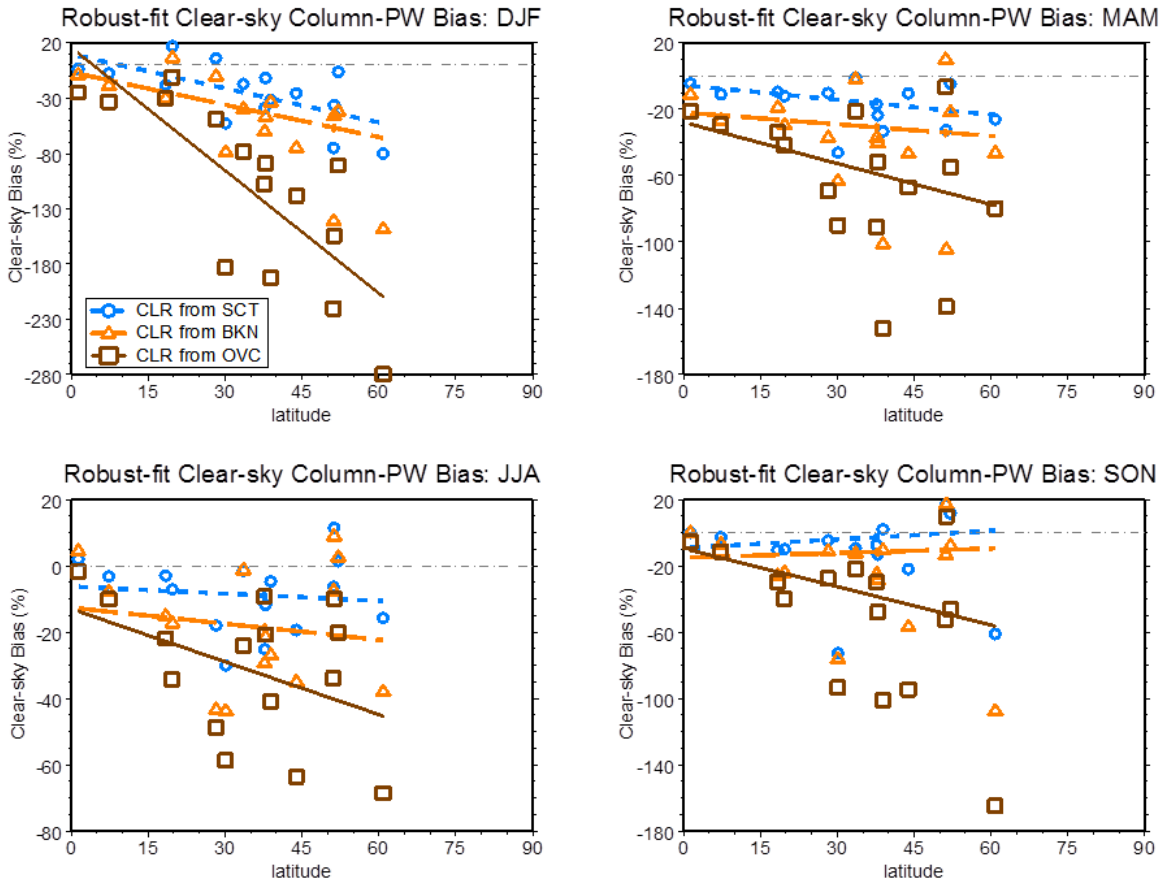

Figure A1. Seasonal clear-sky column water vapor (PW for precipitable water) bias, C01, C02 and C03, as defined in Eqs. (A1), (A2) and (A3). Negative values mean underestimates. The robust-fitting lines are also shown.

Figure A2.

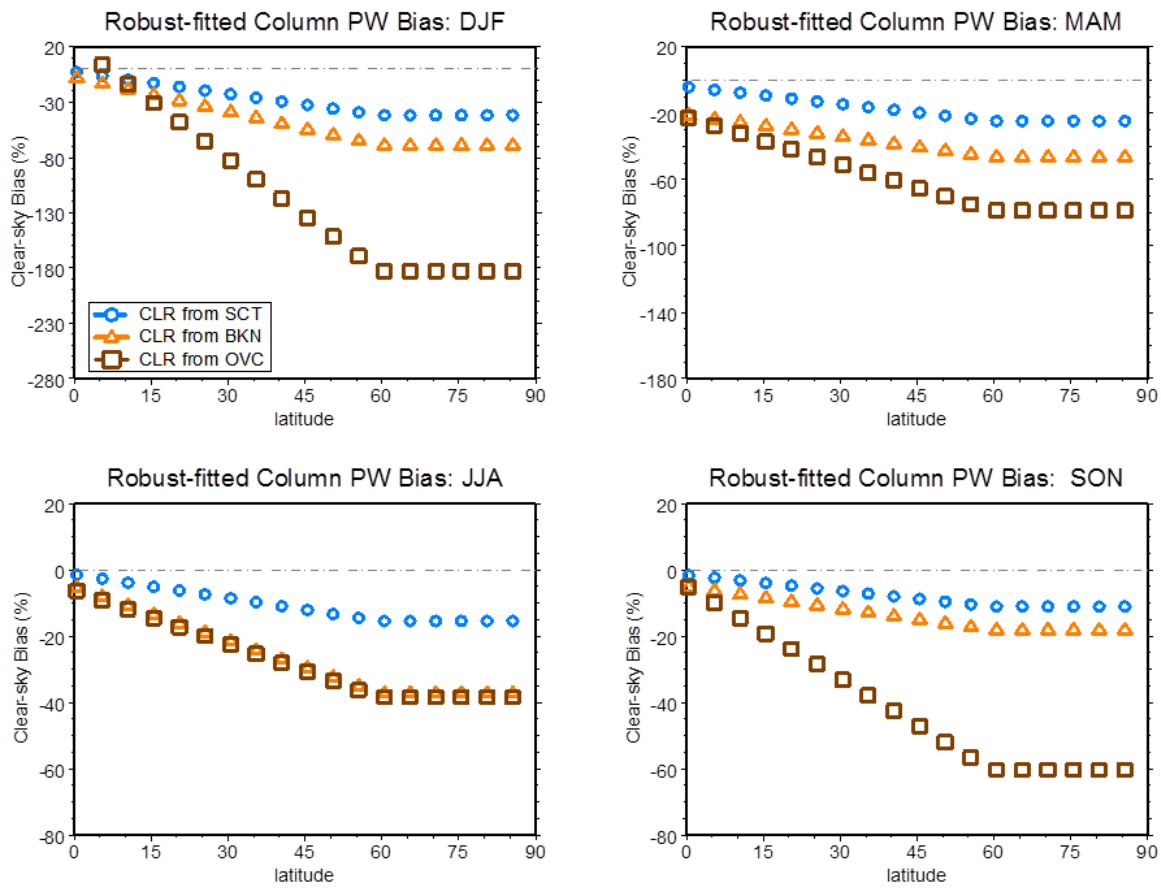

Figure A2. Robust-fitted, seasonal clear-sky column water vapor bias, C01, C02 and C03 as defined in Eqs. (A1), (A2) and (A3), with 60° values extended to the north pole.

With the climatology as shown in Figure A2, we recalculate our CRKs for 4 test versions, N0, N1, N2 and N3 for eight UTCs of the 15th for 12 months (of 2007, as used for FH CRK calculation) and their daily means are taken as pseudo-monthly averages to save CPU time but the results are sufficient for the sensitivity study. The version N0 is equivalent to FH to serve as a comparison base and its mean values are very close to its true-monthly-mean counterparts in Table 2, which justify the pseudo-monthly mean method. The versions N1, N2 and N3 are

calculated with the added dry-bias-corrected column water vapor for SCT, BKN and OVC, respectively, for all the cloud-free layers under the cloud layers. In the sensitivity tests, we set two rational physical restrictions: (1) the total added water vapor (for the saturation and for the cloud-free layers under clouds) is not allowed to be greater than the total dry-bias correction amount (calculated from the dry-bias-correction ratios) and (2) the relative humidity of the said cloud-free layers (under cloud layers) is not allowed to be greater than 95% because of cloud free.

Tables A1 and A2 show the sensitivity study results for TOA and SFC, respectively. Table A1 indicates that the newly added water vapor has negligible effects on TOA CRKs, even for the extreme case for the pair of N3 vs. N0 (the largest possible bias effect but exaggerated), compared with the TOA CRK uncertainties (Table 2). We have also examined zonal-mean plots for thin clouds (that may be affected most) for all N0, N1, N2 and N3 for TOA CRKs and there is virtually no visible difference (not shown). For SFC CRKs, all the errors caused by the water vapor changes are still within the TOA CRK uncertainties (Table 2 and Table S1). However, as expected and shown in Figure A3, the zonal means for the SFC LW CRK for high clouds with thin τ do show large differences (there are virtually no visible differences for medium and thick τ). In the extreme case, the difference between N3 and N0 can be larger than the TOA CRK RMS values, by 45% (or 20% for the RMS in Table S1 in SI), which is certainly overestimated. This is consistent with the uncertainty values of SFC radiative fluxes, which are about double their TOA counterparts (Section 2; Zhang et al., 2021).

Given the CRK uncertainty only contribute < 2% of the uncertainty of the TOA cloud feedback, it seems conclusive that the water vapor change for cloud-free layers under clouds has only higher-order effects on all (TOA, SFC and ATM) CRKs. The reasons may be (1) the water

vapor change is small compared with the original total column vapor and (2) The ISCCP-FH CRK calculation has saturated water vapor within cloud layers that has largely made the water vapor correction. The dry-bias of the under-clouds water vapor may be one day taken into account by CRK calculation if a higher accuracy is needed and if there are available datasets for global column water vapor under different cloud covers.

Figure A3.

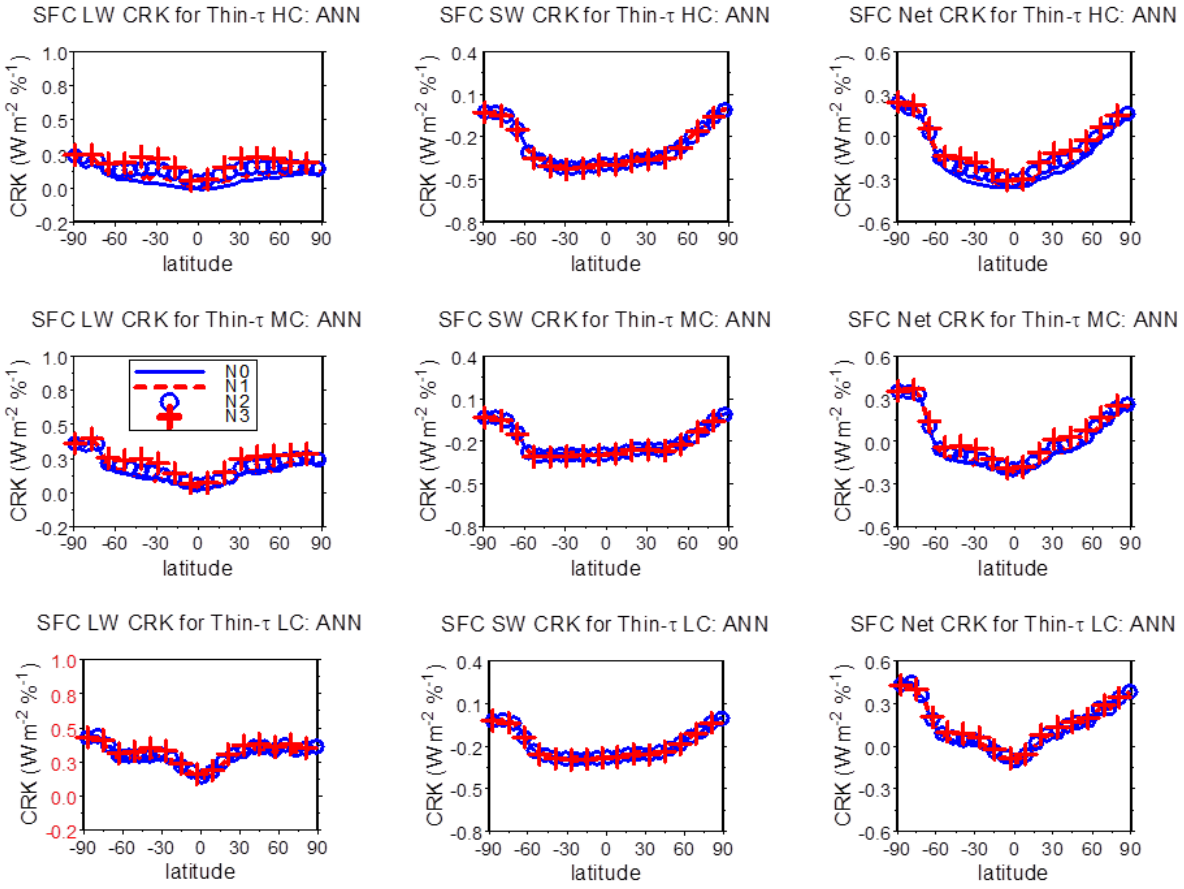

Figure A3. Same as Figure 4a, but for dry-bias water vapor sensitivity tests, N0, N1, N2 and N3 for the four cloud scenarios, CLR, SCT, BRK and OVC, respectively (see Text).

APPENDIX B.

CRK uncertainties due to differences of cloud layer thickness

There is a concern about how much effect on CRKs would be caused by the different cloud thickness between Z2012 and FH. To address this issue, we have conducted another sensitivity study in the same way as described in Appendix A, but only for a new version of NO for Z2012-like cloud thickness to compare with N0 (≈ FH, see Appendix A). In NO, we change N0's cloud thickness to an invariant cloud thickness of 50 hPa as an approximate representation of Z2012's cloud thickness (since most GCM models have 20 vertical layers and we do not have such information from Z2012), but everything else is unchanged. The comparison between NO and N0 is then for the fixed cloud layer thickness of 50 hPa vs. FH's climatological thickness (as exemplified in Figures S1 and S2 in SI). The CRK comparison results show that the two versions (NO minus N0) have mean difference (stdv) of 0.018 ().026), -0.011 (0.013) and 0.007 (0.028) for LW, SW and Net, respectively, for TOA CRKs. For SFC CRKs, they are respectively -0.055 (0.062), 0.004 (0.004) and -0.051 (0.061). The largest effect appears in the SFC LW CRK, about three times the TOA's with opposite sign. These statistical values are consistent with the previous cloud thickness sensitivity studies reported in Zhang et al. (2004).

As the global mean of the TOA CRK differences caused by the cloud thickness difference between Z2012-like and FH are much smaller than the CRK uncertainty values (cf. Table 2), the effect may be taken as secondary. In zonal mean plots for the TOA LW CRKs (similar to the left column in Figures 4a and 4b, not shown), NO has slightly higher values than

N0 for high clouds with thin τ, but the differences can hardly be visible for all the other scenarios (all middle and low clouds, and high clouds with medium-to-thick τ).

Acknowledgments, Samples, and Data

We are deeply indebted to Dr. Mark D. Zelinka who has contributed many valuable ideas as well as supplied his cloud radiate kernel and CFMIP1 datasets that make this paper possible. The CERES FluxByCldTyp-month data were obtained from the NASA Langley Research Center CERES ordering tool at https:/ceres.larc.nasa.gov/data/. The ISCCP-FH cloud radiative kernel data was conducted on NOAA NCEI computer. This study is supported by the NASA MAP program (grant NNH10ZDA001N) and the NASA IDS program (award 19-IDS19-0059). We thank the three anonymous reviewers for their many beneficial and important comments, critiques, suggestions and questions that help improve the paper. The corresponding author also thanks Dr. William B. Rossow for many helpful suggestions and comments, especially on the ISCCP products.

CERES SSF FluxByCldTyp data can be ordered using DOI: 10.5067/Terra-Aqua/CERES/FLUXBYCLDTYP-MONTH_L3.004A. For Data Quality Summary, see https://ceres.larc.nasa.gov/documents/DQ_summaries/CERES_FluxByCldTyp_Ed4A_DQS.pdf.

CERES SYN1deg Ed4 data may also be ordered from https://ceres.larc.nasa.gov/data/#syn1deg-level-3, and for data Quality Summary, see https://ceres.larc.nasa.gov/documents/DQ_summaries/CERES_SYN1deg_Ed4A_DQS.pdf

The CFMIP1 model datasets and MZ (model based) CRK datasets are from the ones used in Zelinka et al. (2012). The OZ (ERA-Interim based cloud radiative kernels) CRK datasets are obtained from Dr. Zelinka, which have been used in Zhou et al. (2013).

The GISTEMP dataset can be downloaded from https://psl.noaa.gov/thredds/catalog/Datasets/gistemp/combined/250km/catalog.html?dataset=Datasets/gistemp/combined/250km/air.2x2.250.mon.anom.comb.nc.

The ISCCP-FH cloud radiative kernel in 2.5 longitude X 2.0 latitude can be downloaded from https://zenodo.org/record/4677580#.YHDsaDwpCUk. Its DOI is 10.5281/zenodo.4677580, which supplies both TOA and SFC CRKs for LW and SW, respectively, from which users can compute ATM CRKs (difference between TOA and SFC) as well as Net CRKs (sum of LW and SW) for all TOA, SFC and ATM.

References

Berry, E., Mace, G. G. & Gettelman, A. (2019). Using A-Train Observations to Evaluate Cloud

Occurrence and Radiative Effects in the Community Atmosphere Model during the Southeast Asia Summer Monsoon, Journal of Climate, 32, 4145-4165, DOI: 10.1175/JCLI-D-18-0693.1.

Bodas-Salcedo, A., Webb, M., Bony, S., Chepfer, H., Dufresne, J., Klein, S., Zhang, Y., Marchand, R., Haynes, J., Pincus, R. &. John, V.O. (2011). COSP Satellite simulation software for model assessment, B. Am. Meteorol. Soc., 92, 1023–1043, https://doi.org/10.1175/2011BAMS2856.1, 2011.

Bony, S., & Dufresne, J. L. (2006). How Well Do We Understand and Evaluate Climate Change Feedback Processes? Journal of Climate, 19, 3445-3482.

CERES Science Team, (2020). CERES_FluxByCldTyp-Day/Month_Ed4A Data Quality Summary, https://ceres.larc.nasa.gov/data/.

Chen, T., Rossow, W. B. & Zhang, Y.-C. (2000). Radiative effects of cloud-type variations. J. Climate, 13, 264–286.

Dessler, A. E. (2010) A determination of the cloud feedback from climate variations over the past decade. Science, 330, 1523–1527, doi:10.1126/science.1192546Dessler, A. E. (2013) Observations of climate feedbacks over 2000–10 and comparisons to climate models. J. Climate, 26, 333–342.

Dessler, A. E. and N. G. Loeb (2013) Impact of dataset choice on calculations of the short-term cloud feedback. J. Geophys. Res., 118, 2821–2826, doi:10.1002/jgrd.50199.

Fu, Q. & Liou, K. N. (1992). On the correlated k-distribution method for radiative transfer in nonhomogeneous atmospheres, J. Atmos. Sci., 49, 2139–2156.

Gaffen, D. J., and Elliott, W. P. (1993). Column water vapor content in clear and cloudy skies, J. Clim., 6, 2278–2287.

GISTEMP Team (2021). GISS Surface Temperature Analysis (GISTEMP), version 4. NASA Goddard Institute for Space Studies. Dataset accessed 20YY-MM-DD at https://data.giss.nasa.gov/gistemp/

Han, Q., Rossow, W. B. & Lacis, A. A. (1994). Near-global survey of effective droplet radii in liquid water clouds using ISCCP data, J. Clim., 7, 465– 497.

Han, Q., Rossow, W. B., Chou, J., Kuo, K.-S. & Welch, R. M. (1999). The effects of aspect ratio and surface roughness on satellite retrievals of ice cloud properties, J. Quant. Spectrosc. Radiat. Trans., 63, 559–583.

Held, I. M. &. Soden, B. J. (2000). Water vapor feedback and global warming. Annu. Rev. Energy Environ., 25, 441–475.

Kato, S. F., Rose, G., Rutan, D. A., Charlock, T. P. (2008). Cloud effects on the meridional atmospheric energy budget estimated from Clouds and the Earth's Radiant Energy System (CERES) data, J. Climate, 21, 4223-4241, DOI: 10.1175/2008JCLI1982.1

Kelley, M., Schmidt, G. A., Nazarenko, L. S., Bauer, S. E., Ruedy, R., Russell, G. L., et al. (2020). GISS‐E2.1: Configurations and climatology. Journal of Advances in Modeling Earth Systems, 12, e2019MS002025. https://doi.org/10.1029/2019MS002025

Kinne, S. (2019). The MACv2 aerosol climatology, Tellus B: Chemical and Physical Meteorology, 71:1, 1-21, DOI: 10.1080/16000889.2019.1623639

Kopp, G., Lawrence, G. & Rottman, G. (2005). The Total Irradiance Monitor (TIM): Science Results, Sol. Phys., 230, 129-140.

Kramer, R. J., Matus, A. V., Soden, B. J., & L'Ecuyer, T. S. (2019). Observation-based radiative kernels from CloudSat/CALIPSO. Journal of Geophysical Research: Atmospheres, 124, 5431–5444. https://doi.org/10.1029/2018JD029021

Lacis, A.A., and Oinas, V. (1991). A description of the correlated k distributed method for modeling nongray gaseous absorption, thermal emission, and multiple scattering in vertically inhomogeneous atmospheres. J. Geophys. Res., 96, 9027-9063, doi:10.1029/90JD01945.

Manabe, S, (1969). Climate and the ocean circulation i-i. the atmospheric circulation and the effect of heat transfer by ocean currents, Monthly Weather Review, Vol. 97, No. 11, Nov. 1969, pp. 775-805.

Ohmura, A. (2014). The Development and the Present Status of Energy Balance Climatology, J. Meteor. Soc. Japan, Vol. 92, No. 4, pp. 245−285, 2014, DOI:10.2151/jmsj.2014-401.

Oreopoulos, L., Cho, N. & Lee, D. (2017). New insights about cloud vertical structure from CloudSat and CALIPSO observations, J. Geophys. Res. Atmos., 122, 9280–9300, doi:10.1002/2017JD026629.

Peixoto, J. P. & Oort, A. H. (1992). Physics of Climate, AIP, 520 pp.Ramanathan, V., Cess, R. D., Harrison, E. F., Minnis, P., Barkstrom, B. R., Ahmad, E.,and Hartmann, D. (1989), Cloud-radiative forcing and climate: Results from the Earth Radiation Budget Experiment, Science, 243, 57–63.Reynolds, R. W. (1988). A real-time global sea surface temperature analysis, J. Clim., 1, 75–86.

Roe, G. H, (2009). Feedbacks, timescales and seeing red. Annu. Rev. Earth. Planet. Sci. 37, 93–115.

Rossow, W. B., Knapp, K. R. and Young, A. H. (2021), International Satellite Cloud Climatology Project: Extending the Record, J. Clim. (accepted).

Rossow, W. B., Walker, A. W., Bueschel, D. & Roiter, M. (1996). International Satellite Cloud Climatology Project (ISCCP) documentation of new cloud datasets, WMO/TD-737, 115 pp., World Clim. Res. Programme, Geneva, Feb.

Rossow, W. B. & Schiffer, R. A. (1999). Advances in understanding clouds from ISCCP, B. Am. Meteorol. Soc., 80, 2261–2288, https://doi.org/10.1175/1520-0477.

Rothman, L.S., Gordon, I.E.,,Babikov, Y., Barbe, A., Benner, Bernath, D. C., et al.(2013). The HITRAN2012 molecular spectroscopic database, J. Quantitative Spectroscopy & Radiative Transfer, 130(2013), 4-50.

Schmidt, G.A., Ruedy, R., Hansen, J. E., Aleinov, I., Bell, N., Bauer, M., et al. (2006). Present day atmospheric simulations using GISS ModelE: Comparison to in-situ, satellite and reanalysis data. J. Climate, 19, 153-192, doi:10.1175/JCLI3612.1.

Shell, K. M., Kiehl, J. T., & Shields, C. A. (2008) Using the radiative kernel technique to calculate climate feedbacks in NCAR's Community Atmospheric Model. Journal of Climate, 21(10), 2269–2282. https://doi.org/10.1175/2007JCLI2044.1

Soden, B.J., Held, I. M., Colman, R., Shell, K. M., Kiehl, J. T. & Shields, C. A. (2008). Quantifying climate feedbacks using radiative kernels. J. Climate, 21, 3504–3520.

Stephens, G. L., Vane, D. G., Boain, R. J., Mace, G. G., Sassen, K., Wang, Z., et al. (2002). The CloudSat mission and the A-train: A new dimension of space-based observations of clouds and precipitation. Bull. Amer. Meteor. Soc., 83, 1771–1790.

Sun, Moguo, Doelling, D.R., Nguyen, L. T., Wilkins, J., & Mlynczak, P. (2019). A New CERES Cloud Type Based Flux Data Product: Algorithm, Validation and Application, American Geophysical Union, Fall Meeting 2019, abstract #A11B-07, Dec. 2019, Bibcode: 2019AGUFM.A11B..07S.

Wang, J., Rossow, W. B. & Zhang, Y.-C. (2000). Cloud vertical structure and its variations from 20-yr global rawinsonde dataset, J. Clim., 12, 3041–3056.

Wang, J. & Rossow, W. B. (1995). Determination of cloud vertical structure from upper-air

observations. J. Appl. Meteor., 34, 2243–2258.

Wielicki, B. A., Barkstrom, B. R., Harrison, E. F., Lee, R. B., Smith, G. L. & Cooper, J. E. (1996)

Clouds and the Earth's Radiant Energy System (CERES): An Earth Observing System experiment, Bull. Am. Meteorol. Soc., 77, 853– 868.

Winker, D. M., Pelon, J. R. & McCormick, M. P. (2003). The CALIPSO mission: Spaceborne lidar for observation of aerosols and clouds. Lidar Remote Sensing for Industry and Environment Monitoring III, U. N. Singh, T. Itabe, and Z. Liu, Eds., International Society for Optical Engineering (SPIE Proceedings, Vol. 4893), 1–11.

Young, A. H., Knapp, K. R., Inamdar, A., Hankins, W. & Rossow, W. B. (2018). The International Satellite Cloud Climatology Project H-Series climate data record product, Earth Syst. Sci. Data, 10, 583-593, https://doi.org/10.5194/essd-10-583-2018, 2018.

Yue, Q., Kahn, B. H., Fetzer, E.T., Schreier, M., Wong, S. Chen, X. & Huang, X. (2016). Observation-based longwave cloud radiative kernels derived from the A-Train. Journal of Climate, 29(6), 2023–2040. https://doi.org/10.1175/JCLI-D-15-0257.1

Zelinka, M. D., Klein, S. A. & Hartmann, D. L. (2012). Computing and partitioning cloud feedbacks using cloud property histograms. Part I: Cloud Radiative Kernels, J. Climate, 25, 3736–3754.

Zelinka, M. D., Myers, T. A., McCoy, D. T., Po-Chedley, S., Caldwell, P. M., Ceppi, P., et al., (2020a). Causes of higher climate sensitivity in CMIP6 models. Geophysical Research Letters, 47, e2019GL085782. https://doi.org/10.1029/2019GL085782

Zelinka, M. D., Myers, T.A., McCoy, D.T., Po-Chedley, S., Caldwell, P.M., Ceppi, P., Klein, S.A. & Taylor, K. E. (2020b) Supporting Information for "Causes of higher climate

sensitivity in CMIP6 models" by Zelinka et al., 2020a (above).

Zhang, Y-C., Rossow, W.B., Lacis, A.A., Mishchenko, M.I. & Oinas, V. (2004). Calculation of radiative fluxes from the surface to top-of-atmosphere based on ISCCP and other global datasets: Refinements of the radiative transfer model and the input data. J. Geophys. Res., 109, doi 10.1029/2003JD004457 (1-27 + 1-25), 2004.

Zhang, Y.-C., Rossow, W. B. & Stackhouse Jr., P. W. (2006). Comparison of different global information sources used in surface radiative flux calculation: Radiative properties of the near-surface atmosphere, J. Geophys. Res., 111, D13106, doi:10.1029/2005JD006873.Zhang, Y.-C., Rossow, W. B., and Lacis, A. A. (1995), Calculation of surface and top of atmosphere radiative fluxes from physical quantities based on ISCCP data sets: 1. Method and sensitivity to input data uncertainties, J. Geophys. Res., 100, 1149–1165.

Zhang, Y.C., Rossow, W.B., Lacis, A.A. and Oinas, V. (2021). Calculation, evaluation and application of long-term, global radiative flux Datasets at ISCCP: Past and present. available (as "Zhang_etal_flux-cal_at-isccp_v4_2021.pdf") under "FH Documentation and Publications" at, https://isccp.giss.nasa.gov/projects/flux.html).

Zhou, C., Zelinka, M. D., Dessler, A. E. & Yang, P. (2013). An analysis of the short-term cloud feedback using MODIS data. J. Climate, 26, 4803–4815, https://doi.org/10.1175/JCLI-D-12-00547.1.

Table 1. The four cloud radiative kernel datasets used for comparison and evaluation.

CRK version	Derived from	Original spatial resolution	Original temporal resolution/coverage	τ X CTP indices	Comparison basis
FH	ISCCP-H + ISCCP-FH code	Global 110-km equal area	3-hourly for a year (of 2007)	7 X 7	12 monthly of τ-CTP histogram on global 280-km equal-area map (equivalent to 2° latitude X 2.5°
CS	MODIS-CERES Observation	Global 1° x 1°	Monthly for 12 months (of 2007)	6 X 7	
MZ	6-model mean states + Fu-Liou code	2° zonal*	Monthly for 12- month climatology	7 X 7	

OZ	ERA-Interim mean states + Fu-Liou code	2.5° zonal*	Monthly for 12- month climatology	7 X 7	longitude equal-angle map)

* In mapping zonal SW CRK to global map, the FH clear-sky surface albedo is used (the CERES surface clear-sky-albedo mapped has minor difference in tests so not used and shown) while zonal LW CRK is simply replicated to all longitudes (i.e., independent of longitudes).

Table 2. Summary of the statistics from comparison of monthly, global and 49- (or 42- for CS associated) bins TOA CRK in Wm^{-2} $\%^{-1}$†

X vs. Y CRKs	X mean	Y mean	Mean difference of (X – Y)	Stdv of (X – Y)	Correlation coefficient	Total equal-area grid cell number
LW Cloud Radiative Kernel						
FH vs MZ	0.514	0.556	-0.043	0.097	0.982	399612
FH vs OZ	0.514	0.549	-0.035	0.094	0.982	399612
MZ vs OZ	0.551	0.544	0.007	0.027	0.999	404348
FH vs CS	0.490	0.510	-0.021	0.176	0.922	260867
MZ vs CS	0.539	0.507	0.032	0.169	0.930	262546
OZ vs CS	0.529	0.507	0.021	0.170	0.928	262546
mean	0.523	0.529	-0.006	0.122	0.957	331589
modulus mean			0.027			
SW Cloud Radiative Kernel						
FH vs MZ	-0.957	-0.998	0.042	0.107	0.993	390251
FH vs OZ	-0.957	-0.991	0.034	0.104	0.993	390251
MZ vs OZ	-0.994	-0.986	-0.008	0.020	1.000	394230
FH vs CS	-0.966	-0.856	-0.110	0.172	0.978	260896
MZ vs CS	-1.010	-0.853	-0.157	0.190	0.977	262518
OZ vs CS	-1.000	-0.853	-0.147	0.187	0.977	262518
mean	-0.981	-0.923	-0.058	0.130	0.986	326777
modulus mean			0.083			
Net (total) Cloud Radiative Kernel						
FH vs MZ	-0.437	-0.436	-0.001	0.118	0.989	390251
FH vs OZ	-0.437	-0.437	0.000	0.115	0.990	390251
MZ vs OZ	-0.436	-0.437	0.001	0.030	0.999	394230
FH vs CS	-0.476	-0.346	-0.130	0.212	0.954	260863
MZ vs CS	-0.471	-0.346	-0.126	0.248	0.941	262484
OZ vs CS	-0.472	-0.346	-0.126	0.248	0.943	262484
mean	-0.455	-0.391	-0.064	0.162	0.969	326760
modulus mean			0.064			

† Each pair's statistics are averaged from their 12-monthly comparison for all bins and 250-km equal-area grid cells (8252 cells for a full map). X and Y are for the 6 possible combinations of the 4 sets of CRKs (Table 1). 'Stdv' is for standard deviation. The modulus (absolute) mean difference (Stdv) for 6 pairs are 0.027 (0.121), 0.083 (0.130) and 0.064 (0.162) Wm^{-2} $\%^{-1}$ for LW, SW and Net, respectively, translated to (bias-included) RMS of 0.124, 0.154 and 0.174 Wm^{-2} $\%^{-1}$ for LW, SW and Net, respectively. Because the same single-layer cloud specification and FU-Liou code are used for both the MZ and OZ CRKs' calculation, they are not completely independent and the above RMS estimates may be underestimated. When the OZ CRKs are removed, the completely independent 3-set CRKs' RMS is increase by ~20% (Table S1 in Supporting Information, SI).

Table 3. Ten global CFMIP1 models used for 2 x CO_2 cloud fraction change experiment†

No.	GCM Climate Models for CMIP1	Abbrev.
1	CCSM3.0* National Center for Atmospheric Research, USA	'n3'
2	HadSM3 Hadley Centre for Climate Prediction and Research/Met Office, UK	'u3'
3	GFDL MLM2.1* NOAA/Geophysical Fluid Dynamics Laboratory, USA	'gf'
4	IPSL CM4* Institute Pierre Simon Laplace, France	'ip'
5	BMRC1* Bureau of Meteorology Research Centre, Australia	'bm'
6	MIROC(hires)* Center for Climate System Research, The University of Tokyo	'mh'
7	MIROC(lowres) Center for Climate System Research, The University of Tokyo	'ml'
8	UIUC University of Illinois at Urbana–Champaign, USA	'ui'
9	HadGSM1 Hadley Centre for Climate Prediction and Research/Met Office, United Kingdom	'ul'
10	HadSM4 Hadley Centre for Climate Prediction and Research/Met Office, United Kingdom	'u4'

†Z2012's Table 1 lists 12 CFMIP1 models, of which only 11 models (excluding MPI ECHAM5) were actually used in Z2012. Of the 11 models, one (AGCM4) has a quality issue so we do not use it (personal communication with Dr. Zelinka). Asterisks denote the 5 models whose atmospheric temperature and specific humidity profiles were unavailable and not used for Z2012's CRKs' calculation. The last column is the abbreviations of the ten models, used in Table S2 in Supporting Information (SI).

Table 4. Uncertainty budget for regional, monthly and bin-mean for TOA cloud feedback, based on RMS of the 4 TOA cloud radiative kernel (Table 2) and the 10 GCM's (normalized) cloud fraction change (CFC) in 2 x CO_2 experiments (Table S2 in SI)†.

CRK from	CRK uncertainty	Mean CFC	CRK uncertainty contribution	Mean CRK	CFC uncertainty	CFC uncertainty contribution	Cloud feedback uncertainty
	δk	ΔC	$\delta k \cdot \Delta C$	k	$\delta(\Delta C)$	$k \cdot \delta(\Delta C)$	$\delta k \cdot \Delta C + k \cdot \delta(\Delta C)$
LW	0.124	0.010	0.00123	0.529	0.332	0.176	0.177
SW	0.154	0.010	0.00154	0.952	0.332	0.316	0.318
Net	0.174	0.010	0.00174	0.423	0.332	0.140	0.142

† k is k_{x_i} for CRK and ΔC is $\frac{dX_i}{dT_s}$ for rate of cloud fraction change with respective to surface air temperature (normalization). Uncertainty of CRK (δk) and CFC [$\delta(\Delta C)$] are RMS from Table 2 and S2 (in SI), respectively. Mean k and mean ΔC are the average of the module X and Y from Table 2 and Table S2 (in SI), respectively. CRK is in $Wm^{-2}\ \%^{-1}$, CFC in $\%K^{-1}$ and cloud feedback in $Wm^{-2}\ K^{-1}$.

Table 5. Minimum and maximum values as range of total cloud feedback (sum of 49 bins) from double CO_2 experiments for global and annual mean of the 10 models using FH CRKs and their ensemble mean (also shown in the title of Figure 6) in W/m^{-2} K^{-1} for TOA, SFC and ATM†

	TOA			SFC			ATM		
	Min	Max	Ensemble	Min	Max	Ensemble	Min	Max	Ensemble
LW	-0.11	0.68	0.20	-0.22	0.00	-0.10	-0.10	0.81	0.30
SW	-0.26	0.86	0.33	-0.21	0.94	0.36	-0.08	0.00	-0.04
Net	0.16	0.89	0.53	-0.34	0.72	0.27	-0.10	0.76	0.26

†Z2012's range of total TOA global mean cloud feedback are -0.13 to 0.69, -0.18 to 0.93 and 0.16 to 0.94 Wm^{-2} K^{-1} for LW, SW and Net, respectively, based on 11 models, of which, 10 models' are shown here. Their ensemble values are 0.21, 0.37 and 0.57 Wm^{-2} K^{-1}, for TOA LW, SW and Net, respectively. The small differences between Z2012's and this study are caused by both model number (11 vs. 10) and CRK difference. The (normalized) CFC range is -0.882 to -0.0002 with ensemble value of -0.47 $\%K^{-1}$ from this study compared Z2012's -0.91 to -0.02 with ensemble value of -0.46 $\%K^{-1}$.

Table 6. Global average of cloud feedback contributions (in Wm^{-2} K^{-1}), partitioned to high, middle and low clouds, and thin-, medium- and thick-τ clouds, respectively†.

a. Partitioned for high, middle and low clouds									
Clouds	LW			SW			NET		
	TOA	SFC	ATM	TOA	SFC	ATM	TOA	SFC	ATM
Total	0.20	-0.09	0.29	0.32	0.35	-0.03	0.52	0.26	0.26
High	0.30	0.04	0.27	-0.18	-0.19	0.01	0.12	-0.15	0.27
Middle	-0.09	-0.06	-0.03	0.24	0.24	-0.01	0.15	0.18	-0.04
Low	-0.01	-0.07	0.06	0.26	0.29	-0.03	0.25	0.22	0.02
b. Partitioned for thin-, medium- and thick-τ clouds									
τ	LW			SW			NET		
	TOA	SFC	ATM	TOA	SFC	ATM	TOA	SFC	ATM
Total	0.20	-0.09	0.29	0.32	0.35	-0.03	0.52	0.26	0.26
Thin	-0.00	-0.10	0.10	0.04	0.05	-0.01	0.04	-0.05	0.09
Medium	0.04	-0.10	0.14	0.30	0.33	-0.04	0.34	0.23	0.11
Thick	0.17	0.11	0.05	-0.03	-0.03	0.01	0.14	0.08	0.06

†The total global average is identical for the two different partitions.

Table 7. Statistis from comparision between CERES and ISCCP-FH CRK-derived cloud radiative effects (in W m^{-2}) based on global, monthly means for years from 2007 to 2016†.

CRE for	X: CERES Mean	Y: FH Mean	Mean Dif of X-Y	Stdv of X-Y	Corr. Coef.	Slope	Intercept	# of months
TOA LW	25.528	22.908	2.619	0.636	0.715	0.757	3.670	120
TOA SW	-45.598	-51.274	5.676	0.680	0.991	1.113	-0.520	120
TOA Net	-20.071	-28.366	8.295	0.585	0.987	1.032	-7.614	120
SFC LW	28.039	23.272	4.767	1.063	0.431	0.392	12.196	120
SFC SW	-50.850	-53.324	2.474	0.627	0.985	0.977	-3.569	120
SFC Net	-22.811	-30.052	7.242	1.031	0.974	1.226	-2.090	120
ATM LW	-2.178	-1.012	-1.166	1.180	0.676	0.443	0.043	120
ATM SW	6.947	3.834	3.114	0.544	0.949	0.431	0.829	120
ATM Net	4.769	2.822	1.947	0.758	0.820	0.841	-1.167	120
mean	-8.469	-12.355	3.885	0.789	0.837	0.801	0.197	120
Abs mean			4.145					

†CERES CREs are based on TOA fluxes from the SSF products and SFC fluxes from the SYN products. FH's CREs are calculated from Σ(CRK*CF) over 42 cloud types (see text for details). The statistical terminologies are the same as Table 2 except that intercept is included (from regression) here.

Table 8. Comparison between CERES and ISCCP-FH CRK-derived cloud feedback (in W m^{-2} K^{-1}) with respect to surface air temperature anomaly (ΔTs) based on slope from linear-least-square regression for global, monthly means for years from 2007 to 2016†.

CERES cloud feedback			FH CRK derived cloud feedback		
LW	SW	Net	LW	SW	Net
TOA					
-0.14 ±0.33	0.36 ±0.49	0.22 ±0.54	0.60 ±0.30	0.26 ±0.51	0.87 ±0.52
SFC					
0.70 ±0.34	0.45 ±0.55	1.15 ±0.51	-0.11 ±0.26	0.27 ±0.55	0.17 ±0.39
ATM					
-0.82 ±0.52	-0.10 ±0.17	-0.93 ±0.45	0.71 ±0.43	-0.02 ±0.08	0.69 ±0.37

†The 95% confidence interval is also shown for uncertainty estimate.

Table A1. Summary of the statistics from comparison of pseudo-monthly, global and 49-cloud types for TOA cloud radiative kernel for sensitivity tests to water vapor content changes under cloud layers in W/(m^2 %)†

Comparison for X vs. Y CRKs	X mean	Y mean	Mean difference of (X – Y)	Stdv	Correlation coefficient	Total equal-area box number
LW Cloud Radiative Kernel						
N3 VS N0	0.515	0.513	0.001	0.009	1.000	399612
N2 VS N0	0.515	0.513	0.001	0.006	1.000	399612
N1 VS N0	0.514	0.513	0.001	0.002	1.000	399612
N3 VS N1	0.515	0.514	0.001	0.007	1.000	399612
N3 VS N2	0.515	0.515	0.000	0.005	1.000	399612
N2 VS N1	0.515	0.514	0.001	0.003	1.000	399612
mean	0.515	0.514	0.001	0.006	1.000	399612
abs m-df	0.515	0.514	0.001	0.006	1.000	399612
SW Cloud Radiative Kernel						
N3 VS N0	-0.932	-0.933	0.001	0.003	1.000	399612
N2 VS N0	-0.933	-0.933	0.001	0.002	1.000	399612
N1 VS N0	-0.933	-0.933	0.000	0.001	1.000	399612
N3 VS N1	-0.932	-0.933	0.001	0.002	1.000	399612
N3 VS N2	-0.932	-0.933	0.000	0.001	1.000	399612
N2 VS N1	-0.933	-0.933	0.000	0.001	1.000	399612
mean	-0.933	-0.933	0.001	0.002	1.000	399612
abs m-df	-0.933	-0.933	0.001	0.002	1.000	399612
Net (total) Cloud Radiative Kernel						
N3 VS N0	-0.418	-0.420	0.002	0.011	1.000	399612
N2 VS N0	-0.418	-0.420	0.002	0.006	1.000	399612
N1 VS N0	-0.419	-0.420	0.001	0.003	1.000	399612
N3 VS N1	-0.418	-0.419	0.001	0.008	1.000	399612
N3 VS N2	-0.418	-0.418	0.001	0.005	1.000	399612
N2 VS N1	-0.418	-0.419	0.001	0.004	1.000	399612
mean	-0.418	-0.419	0.001	0.006	1.000	399612
abs m-df	-0.418	-0.419	0.001	0.006	1.000	399612

† Similar to Table 2, but the statistics are based on daily average of the 15th of 12 months, used as pseudo-monthly average. X and Y are for 6 possible pairs for comparing the four sets of CRKs, N0, N1, N2 and N3, where N0 ≈ FH; N1, N2 and N3 have increased water vapor for cloud-free layers underneath cloud layers for dry-bias correction with respect to N0's water vapor content underneath the cloud layers for SCT, BKN and OVC scenarios respectively (see Appendix A for details). The modulus mean of mean difference (Stdv) for 6 pairs are 0.001 (0.006), 0.001 (0.002) and 0.001 (0.006) W/(m^2 %) for LW, SW and Net, respectively. They are translated to bias-included RMS of 0.006, 0.002 and 0.006 W/(m^2 %) for LW, SW and Net, respectively. The first pair (N3 vs N0) has the largest RMS, 0.009, 0.003 and 0.011 for LW, SW and Net, respectively, as expected, which are negligibly small with respect to TOA CRKs' (Table 2).

Table A2. Summary of the statistics from comparison of pseudo-monthly, global and 49-cloud types for SFC cloud radiative kernel for sensitivity tests to water vapor content changes under cloud layers in W/(m^2 %)†

Comparison for X vs. Y CRKs	X mean	Y mean	Mean difference of (X – Y)	Stdv	Correlation coefficient	Total equal-area box number
LW Cloud Radiative Kernel						
N3 VS N0	0.332	0.265	0.067	0.064	0.961	399612
N2 VS N0	0.301	0.265	0.037	0.039	0.987	399612
N1 VS N0	0.277	0.265	0.013	0.018	0.997	399612
N3 VS N1	0.332	0.277	0.054	0.050	0.974	399612
N3 VS N2	0.332	0.301	0.030	0.036	0.984	399612
N2 VS N1	0.301	0.277	0.024	0.024	0.995	399612
mean	0.313	0.275	0.038	0.039	0.983	399612
abs m-df	0.313	0.275	0.038	0.039	0.983	399612
SW Cloud Radiative Kernel						
N3 VS N0	-0.994	-0.986	-0.007	0.010	1.000	399612
N2 VS N0	-0.991	-0.986	-0.005	0.007	1.000	399612
N1 VS N0	-0.988	-0.986	-0.002	0.003	1.000	399612
N3 VS N1	-0.994	-0.988	-0.006	0.008	1.000	399612
N3 VS N2	-0.994	-0.991	-0.003	0.004	1.000	399612
N2 VS N1	-0.991	-0.988	-0.003	0.004	1.000	399612
mean	-0.992	-0.988	-0.004	0.006	1.000	399612
abs m-df	-0.992	-0.988	0.004	0.006	1.000	399612
Net (total) Cloud Radiative Kernel						
N3 VS N0	-0.662	-0.722	0.060	0.057	0.998	399612
N1 VS N0	-0.711	-0.722	0.011	0.016	1.000	399612
N3 VS N1	-0.662	-0.711	0.049	0.045	0.999	399612
N3 VS N2	-0.662	-0.690	0.027	0.033	0.999	399612
N2 VS N1	-0.690	-0.711	0.021	0.021	1.000	399612
mean	-0.679	-0.713	0.033	0.035	0.999	399612
abs m-df	-0.679	-0.713	0.033	0.035	0.999	399612

† Same as Table A1, but for SFC cloud radiative kernels. The modulus mean of mean difference (Stdv) for 6 pairs are 0.038 (0.039), 0.004 (0.006) and 0.034 (0.035) W/(m^2 %) for LW, SW and Net, respectively. They are translated to bias-included RMS of 0.054, 0.002 and 0.048 W/(m^2 %) for LW, SW and Net, respectively. The first pair (N3 vs N0) has the largest RMS, 0.093, 0.012 and 0.082 for LW, SW and Net, respectively, as expected, which are within the uncertainty ranges of the TOA CRKs' (Table 2 and Table S2).